

# JGR Solid Earth

## RESEARCH ARTICLE

10.1029/2024JB029143

### Key Points:

- Ten years (2013–2023) quantification of heat flux VRPSWIR from active craters at Stromboli using Sentinel-2 and Landsat-8/-9 SWIR images
- Two main thermal clusters emitting  $\sim 12 \times 10^{14}$  J. Thermal increase since April 2017 marks a reactivation of intense Strombolian activity
- NE, C, and SW craters show distinct thermal behavior, with the NE as the most energetic. VRP<sub>SWIR</sub> tracks transition to more explosive phases

### Supporting Information:

Supporting Information may be found in the online version of this article.

### Correspondence to:

F. Massimetti,  
francesco.massimetti@unito.it

### Citation:

Massimetti, F., Laiolo, M., Aiuppa, A., Aveni, S., Bitetto, M., Campus, A., et al. (2024). Thermal emissions of active craters at Stromboli Volcano: Spatio-temporal insights from 10 years of satellite observations. *Journal of Geophysical Research: Solid Earth*, 129, e2024JB029143. <https://doi.org/10.1029/2024JB029143>

Received 19 MAR 2024

Accepted 26 JUL 2024

### Author Contributions:

**Conceptualization:** F. Massimetti, M. Laiolo, D. Coppola

**Data curation:** F. Massimetti, M. Laiolo, A. Aiuppa, S. Aveni, M. Bitetto, A. Campus, M. Coltelli, A. Cristaldi, D. Delle Donne, L. Innocenti, G. Lacanna, E. Privitera, M. Ripepe, G. Salerno, D. Coppola

**Formal analysis:** F. Massimetti

**Investigation:** F. Massimetti, M. Laiolo, D. Coppola

**Methodology:** F. Massimetti

**Project administration:** D. Coppola

**Software:** F. Massimetti


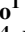


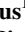



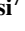




**Supervision:** M. Laiolo, D. Coppola

© 2024. The Author(s).

This is an open access article under the terms of the [Creative Commons Attribution License](#), which permits use, distribution and reproduction in any medium, provided the original work is properly cited.

Attribution License, which permits use, distribution and reproduction in any medium, provided the original work is properly cited.

# Thermal Emissions of Active Craters at Stromboli Volcano: Spatio-Temporal Insights From 10 Years of Satellite Observations

F. Massimetti<sup>1</sup> , M. Laiolo<sup>1</sup> , A. Aiuppa<sup>2</sup> , S. Aveni<sup>1,3</sup>, M. Bitetto<sup>2</sup> , A. Campus<sup>1</sup> , M. Coltelli<sup>4</sup> , A. Cristaldi<sup>4</sup>, D. Delle Donne<sup>5</sup>, L. Innocenti<sup>6</sup> , G. Lacanna<sup>6</sup> , M. Pistolesi<sup>7</sup> , E. Privitera<sup>4</sup> , M. Ripepe<sup>6</sup> , G. Salerno<sup>4</sup> , and D. Coppola<sup>1</sup> 

<sup>1</sup>Department of Earth Science, University of Turin, Torino, Italy, <sup>2</sup>Department of Earth and Marine Sciences, University of Palermo, Palermo, Italy, <sup>3</sup>Department of Civil, Constructional and Environmental Engineering, Sapienza University of Rome, Roma, Italy, <sup>4</sup>Istituto Nazionale di Geofisica e Vulcanologia, Osservatorio Etneo, Catania, Italy, <sup>5</sup>Istituto Nazionale di Geofisica e Vulcanologia, Osservatorio Vesuviano, Napoli, Italy, <sup>6</sup>Department of Earth Science, University of Florence, Firenze, Italy, <sup>7</sup>Department of Earth Science, University of Pisa, Pisa, Italy

**Abstract** Open-vent volcanoes continuously emit magmatic products and frequently feature multiple adjacent craters. Temporal shifts of thermal emissions between craters are especially detectable by InfraRed satellites. Here, SENTINEL-2 and LANDSAT-8/9 Short Wave InfraRed (SWIR) high-spatial resolution satellite data, are combined to investigate 10 years (2013–2023) of thermal activity at Stromboli volcano (Italy). The correlation between Volcanic Radiative Power (VRP, in Watts) and Volcanic Radiative Energy (VRE, in Joules), retrieved by moderate MODIS and VIIRS Middle InfraRed (MIR) data, with the Thermal Index SWIR (TI<sub>SWIR</sub>) data, allows us to quantify long-term series of heat fluxes (VRP<sub>SWIR</sub>) and energy (VRE<sub>SWIR</sub>). Combining moderate and higher spatial resolution data and fitting cumulative trends of TI<sub>SWIR</sub> with VRE<sub>MIR</sub> allows to measure thermal activity sourced by single craters during Strombolian activity. Long-term results highlight that thermal emissions are clustered in the northern and southern parts of the crater terrace, with total energy emitted ( $\sim 12 \times 10^{14}$  J) equally distributed. The thermal increase since April 2017 marked a reactivation of shallow magma transportation and an intensification of the activity after the 2014 eruption. Distinct thermal behaviors are shown by the NE, C, and SW craters, related to mechanisms of explosions. We found that short-term thermal variations match well those resolved by ground-based signals, and the NE crater as the most sensitive to the transition to higher-intensity activity. Our multispatial/multisensory investigation allows, for the first time, the long-term quantification of heat flux from Stromboli's craters, with an improved understanding of open-vent dynamics and a new approach to monitor multiple active craters.

**Plain Language Summary** Stromboli is a volcano in southern Italy, historically well-known, considered unique and fascinating for its persistent emission of magma and gas through multiple adjacent craters lasting for millennia. This study focuses on tracking the thermal activity of Stromboli using modern satellite data over 2013–2023, with unprecedented levels of detail able to distinguish the heat released by single craters. The analysis revealed that most thermal emissions at Stromboli were concentrated in two primary sectors of the summit terrace. Notably, a significant increase in thermal activity was observed since April 2017, indicating a resurgence in volcanic activity after a period of relatively calm following the previous eruption. Distinct thermal behaviors of the three historically active craters of Stromboli have been recognized and reconciled with different styles of volcanic explosions. Furthermore, the study identified patterns of heat release within Stromboli's main craters which agreed with the fluctuations in gas emissions and explosive activity characterizing the volcano. Overall, this comprehensive analysis provides valuable insights to scientists and volcano-involved communities into the long-term quantification of heat flux from multiple craters at Stromboli, contributing to a better understanding of open-vent eruptive dynamics and enhancing continuous monitoring of Stromboli and similar volcanoes.

## 1. Introduction

Open-vent volcanoes are natural systems exhibiting a continuous and shallow-level magmatic circulation, lasting years to millennia (Edmonds et al., 2022; Vergnolle & Métrich, 2021). These are broadly characterized by an almost persistent exposure of the magmatic column, coupled with continuous degassing and background

**Validation:** F. Massimetti  
**Visualization:** F. Massimetti  
**Writing – original draft:** F. Massimetti  
**Writing – review & editing:** M. Laiolo, A. Aiuppa, S. Aveni, D. Delle Donne, G. Lacanna, M. Pistolesi, D. Coppola

seismicity (Rose et al., 2013; Vergnolle & Métrich, 2022). Open-vent volcanoes are also significant emitters of heat (Coppola et al., 2020; Francis et al., 1993; Harris & Stevenson, 1997a; Kazahaya et al., 1994; Laiolo et al., 2022; Valade et al., 2023; Wright et al., 2015), particularly at low-viscosity systems, where convecting shallow magma circulation feeds mild explosive activity (Strombolian), lava lakes, or lava flows (Aiuppa et al., 2018; Campion & Coppola, 2023; Harris & Stevenson, 1997a; Rose et al., 2013).

These volcanoes often exhibit bimodal volcanic behavior, with mild, regular activity occasionally interrupted by more violent, hazardous explosions and/or major effusive eruptions (Houghton & Gonnermann, 2008; Rose et al., 2013; Rosi et al., 2013; Vergnolle & Métrich, 2021). Detecting mid-to long-term precursory signals to these major eruptions is a challenging task (Acocella et al., 2024; Smittarello et al., 2022; Viccaro et al., 2021), mainly because variations in the main monitored parameters for open-vent volcanic activity (i.e., tremor amplitude, seismic LP and VLP signals, number of explosions, plume height, SO<sub>2</sub> flux, infrasonic pressure, deformation patterns, thermal anomalies; Reath et al., 2019; Rose et al., 2013; Vergnolle & Métrich, 2022) can be so subtle to be hardly resolvable from background activity changes (Tilling, 2008), and/or because signals can become clearly resolvable with short advance (days to minutes) before large explosions (Aiuppa et al., 2021; Di Lieto et al., 2020; Giudicepietro et al., 2023; Ripepe, Lacanna, et al., 2021). In open-vent volcanoes, some thermal precursor signals of substantial changes in volcanic activity have been observed in some cases at Stromboli (Calvari et al., 2022; Giudicepietro et al., 2020), Ambrym (Marchese, Coppola, et al., 2022; Marchese, Genzano, et al., 2022), Bezymianny (van Manen et al., 2010) and Etna (Calvari, Bonaccorso, et al., 2021; Calvari, Giudicepietro, et al., 2021; Laiolo et al., 2019), among others; however, the mere presence of thermal activity to a volcano does not necessarily constitute a change from its background level or evidently mark the transition to violent and major eruptive phases. Improving the chances of forecasting rapid increases in eruptive activity in open-vent volcanoes requires continuous and detailed monitoring of geophysical, geochemical, and thermal parameters, to produce the most continuous and reliable data sets (Chaussard et al., 2013; Coppola et al., 2019, 2023; Phillipson et al., 2013; Valade et al., 2016); indeed, the availability of solid long-term data sets is essential to establish, with early notice, whether the volcanic system is deviating from its long-term baseline activity (Phillipson et al., 2013; Reath et al., 2019; Sparks, 2003).

Several open-vent volcanoes are also prone to modifications in the number and location of active vents, due to the interplay between evolving morphologies and eruptive dynamics and intensities (Rose et al., 2013; Salvatore et al., 2018; Simons et al., 2020). In some contexts, several vents (hereafter defined as single volcanic orifices emitting eruptive products) can cluster within multiple craters (larger sub-circular morphological units, which can contain multiple vents), as in the case of Stromboli and Etna (Italy; Behncke et al., 2014; Rosi et al., 2013), Ambrym and Yasur (Vanuatu; Németh & Cronin, 2008; Woitischek et al., 2020), Erta Ale (Ethiopia; Barnie et al., 2016), and so on. The presence of multiple craters, rather than a single emitting one, is indicative of a complex shallow conduit system, whose structure can change over time. Activity shifts from one crater to another have sometimes been interpreted as indicative of imminent variations in the volcano's state (Delle Donne et al., 2022; Ripepe et al., 2009; Zuccarello et al., 2022). It has been shown that parameterizing the activity patterns at each vent can give relevant information about shallow conduit dynamics (Giberti et al., 1992), thermal budgets (Harris & Stevenson, 1997b), source mechanisms of explosions (Chouet et al., 2003; McGreger & Lees, 2004; Ripepe & Marchetti, 2002; Salvatore et al., 2018), degassing processes (Delle Donne et al., 2022; Tamburello et al., 2012), and eruptive dynamics (Cannata et al., 2011; Ripepe et al., 2008). Besides, the interpretation of these patterns was found key to identify precursory signals before paroxysms (Zuccarello et al., 2022), this, in turn, essential for hazard mitigation purposes (Johnson et al., 2018; Ripepe et al., 2018). Nevertheless, the proximity among craters makes it difficult to discriminate the source of the emissions (i.e., magma, gas, or heat), owing to insufficient resolution of the used instruments, morphological complexities, and diversity of eruptive styles occurring from different craters (Andronico et al., 2021; Ripepe et al., 2008). Tracking spatial variations for long periods requires advanced monitoring techniques (often from proximal stations) that allow the discrimination of the activity of each crater.

Thermal emissions, and more specifically the emitted heat flux, are key parameters to study active volcanoes (Coppola et al., 2020; Francis, 1979; Harris, 2013; Reath et al., 2019; Wright & Flynn, 2003; Wright & Pilger, 2008; Yokoyama, 1972). At open-vent volcanoes, it has been suggested that heat flux is proportional to the flux of magma (and gas) that is superficially discharged (erupted) and/or that circulates within the very shallow magmatic system (Campion & Coppola, 2023; Coppola et al., 2012; Harris & Stevenson, 1997a; Laiolo et al., 2022; Valade et al., 2016). This makes heat flux an excellent proxy of shallow volcanic processes, and an

especially sensitive parameter to track the fluctuations of the magmatic column within the upper portion of the system, which can ultimately trace the transition into higher intensity or effusive activity (Coppola et al., 2012; Laiolo et al., 2022). Even at well-monitored volcanoes, thermal investigations benefit from space-based data that have now been safely acquired for decades, building robust, homogenous, and stable data sets (Coppola et al., 2020, 2023). The recent availability of higher spatial resolution InfraRed imagery (<90 m/pixel; Blackett, 2017; Harris, 2013; Ramsey et al., 2022) makes it possible to localize the position of active craters with decametric precision, and to characterize the magnitude and spatial information of any Volcanic Thermal Feature (VTF; hereby defined as a sub-pixel spatial element with temperatures above the background) (Coppola et al., 2023; Flynn et al., 2001; Laiolo et al., 2019; Marchese et al., 2018; Massimetti et al., 2020; Mia et al., 2018; Oppenheimier et al., 1993; Plank et al., 2019; Rothery et al., 1988).

Stromboli volcano (Italy), represents one of the most iconic open-vent volcanoes worldwide, exhibiting continuous thermal emissions from multiple craters (Coppola et al., 2012; Giberti et al., 1992; Ripepe et al., 2008; Rosi et al., 2013). This volcano has been the subject of extensive research on thermal activity through satellite methods (see Calvari et al., 2022; Coppola et al., 2012; Gaonac'h et al., 1994; Harris & Stevenson, 1997b; Laiolo et al., 2022; Plank et al., 2019; Wright et al., 2015). Some of the studies focused on the analysis of the bulk thermal activity (in terms of heat flux or number of hot-spot contaminated pixels), or derived parameters such as Time Average Lava Discharge Rate (TADR) in m<sup>3</sup>/s (cf. Coppola et al., 2016; Ganci et al., 2016; Marchese et al., 2019; Massimetti et al., 2020). Nevertheless, a long-lasting quantification of heat flux produced by single craters at Stromboli has never been performed systematically so far; a few attempts have proposed to qualitatively differentiate activity at the crater scale using diverse satellites for single eruption (i.e., Laiolo et al., 2019; Marchese et al., 2018), while older investigations integrated ground and space-based techniques to map and quantify heat emissions at crater extent (Harris & Stevenson, 1997a). One aspect that has received little attention so far is whether thermal activity differs between craters and how these variations are related to the eruptive dynamics and the movement of magma/gas within a branched conduit system.

Here, we analyze 10 years of satellite InfraRed images, acquired by multiple sensors at Stromboli volcano from April 2013 to July 2023. We combine measurements from moderate resolution sensors (375–1,000 m), acquiring data in the Middle InfraRed (MIR; 3–5  $\mu\text{m}$ ), with higher resolution sensors (20–30 m), acquiring in the Short Wave InfraRed (SWIR: 1–3  $\mu\text{m}$ ), to track the variations of the heat emissions from single craters. This multi-sensory approach allows us to: (a) trace variations in the position and intensity of the thermal activity at each crater; (b) estimate the heat flux baseline produced by each crater; (c) evaluate the long-term thermal energy emission for different crater sectors. Finally, we compare our thermal data set to other ground-based geophysical and geochemical parameters, in an attempt to link the thermal patterns at individual craters with changes in volcanic activity and in the efficiency of magma circulation in the shallow feeding system.

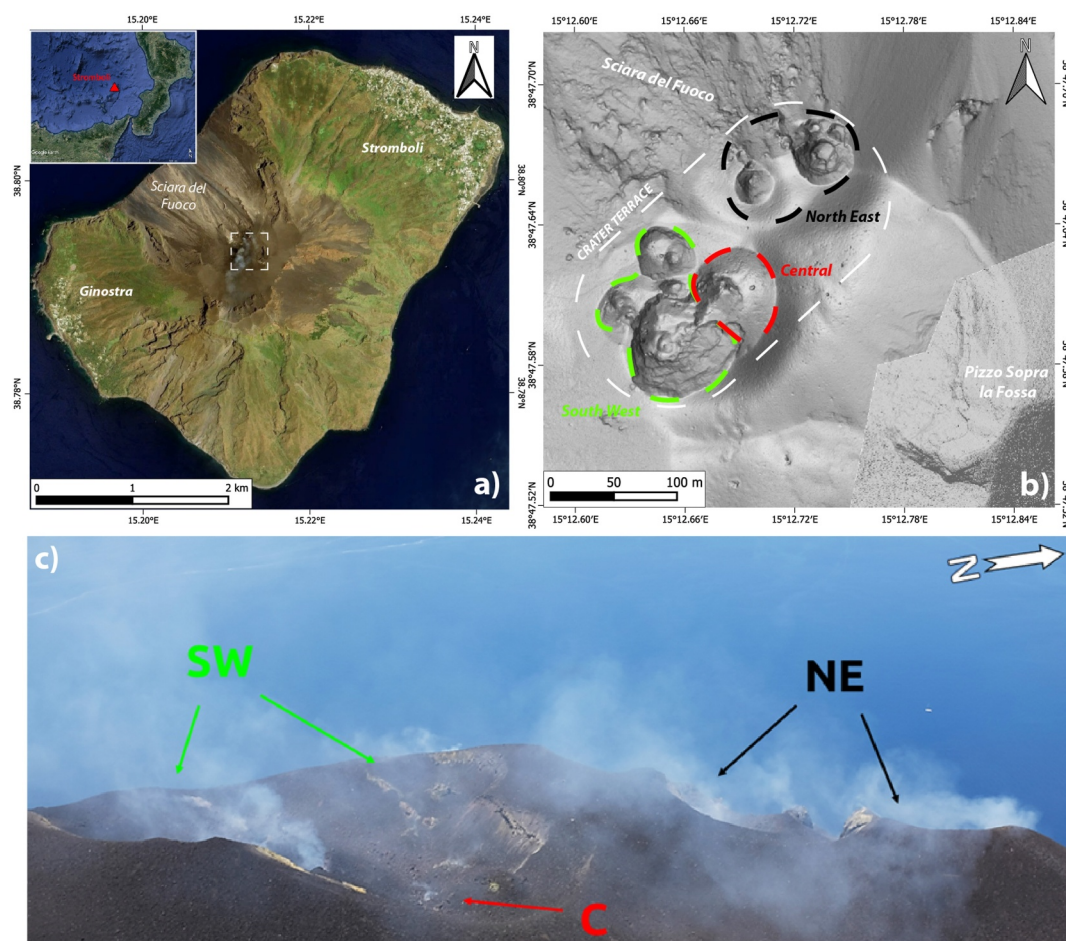
## 2. Stromboli Volcano

### 2.1. Stromboli's Eruptive Activity

Stromboli volcano (Aeolian Islands, Southern Italy, 924 m a.s.l., Figure 1) is a world-renown archetype of an open-vent system, for its regular, millennial-lasting, and mild explosive Strombolian activity, also termed “ordinary” (Mercalli, 1907; Rosi et al., 2000, 2013). This activity occurs from several vents, or three main craters clustered within a crater terrace, an oval-shaped structure 300  $\times$  50 m in size, located at ca. 780 m a.s.l. in the upper portion of the Sciara del Fuoco (SdF, a collapsed sector delimited by a horseshoe scarp; Calvari, Bonaccorso, et al., 2021; Calvari, Giudicepietro, et al., 2021; Rosi et al., 2013; Tibaldi et al., 2008). It ranks among the most studied open-vent volcanoes in the world (Allard et al., 1994; Ripepe et al., 2008) and one of the most visited (Andronico et al., 2021).

Stromboli's regular activity (ordinary) is characterized by continuous degassing accompanied by repetitive and mild explosions, ejecting bombs, black scoriae, lapilli, and ash. These explosions occur with a frequency of  $\sim$ 10 events/h and have a duration of a few seconds (up to 30 s) while erupted tephra masses of 10–10<sup>4</sup> kg (corresponding to volumes of 1–10 m<sup>3</sup>) reach 50–400 m above the active vents (see Barberi et al., 1993; Harris et al., 2013; Patrick et al., 2007; Ripepe et al., 2008; Rosi et al., 2013). This ordinary activity is thought to be sustained by a steady-state convective regime within the shallow, upper portion of the magmatic conduit (<3 km depth; Allard et al., 1994), where a relatively gas-rich magma ascends, degases, crystallizes, and then sinks back (Aiuppa et al., 2010; Allard et al., 2008). Accordingly, most of the magma remains unerupted (Allard et al., 1994;





**Figure 1.** Setting of Stromboli volcano. (a) View of Stromboli island, by Landsat-8 OLI Visible image of July 2023; (b) DEM of the summit area of Stromboli focused on the summit area, with the localization of NorthEast, Central, and SouthWest crater sectors inside the crater terrace (July 2022); (c) photo taken from Pizzo sopra la Fossa looking at crater terrace, June 2023.

Shinohara, 2008), and only a small portion is erupted through mild summit explosions (Harris & Stevenson, 1997a). Although this mechanism is defined as steady, with an averaged magma supply rate of  $0.1\text{--}0.5\text{ m}^3/\text{s}$  (Allard et al., 2008; Burton et al., 2007), the activity is highly variable even over a daily scale, with variations in gas flux, magma level, explosive frequency, and thermal emissions (Aiuppa et al., 2010; Ripepe et al., 2008).

Sharp deviations from this mild explosive activity occur during effusive eruptions or more energetic and violent events, such as major and paroxysmal explosions, which pose increased hazards for the inhabitants of local villages, tourists, and scientists (Barberi et al., 1993; Ripepe et al., 2008; Ripepe, Lacanna, et al., 2021; Rosi et al., 2013). These eruptive episodes span a wide range in magnitude and intensity; effusive eruptions can occur as: (a) short-lived lava effusions having small to intermediate volumes ( $10^5\text{--}10^6\text{ m}^3$ ) produced by the summit craters, called lava overflows (Rosi et al., 2013), and (b) large-volume effusive eruptions ( $10^7\text{ m}^3$ ) fed either by flank fissures opened along the volcano's flanks, remaining active for months, as observed on 2002–2003, 2007, and 2014 (Barberi et al., 2009; Ripepe et al., 2017), or fed directly from summit craters as in July 2019 (Giordano & De Astis, 2021; Laiolo et al., 2022). Violent explosive events are classified as major explosions and paroxysms (Barberi et al., 1993), both characterized by the activation of more than one vent and by ballistic and tephra fallout on the upper part of the volcanic edifice, occasionally reaching the inhabited villages along the coast (Rosi et al., 2013). Averaged recurrence times of major explosions and paroxysms are 2.1 and 0.16 events/year in the last 25 years, respectively (Bevilacqua et al., 2020). These explosive events span a wide range of durations (from less than 2 min to 5–10 min), erupted masses (of  $10^4\text{--}10^9\text{ kg}$ ) and volumes (up to  $10^6\text{ m}^3$ ), and produce eruptive columns ranging in height from a few hundreds of meters to 8 km (Bertagnini et al., 2011; Giordano & De

Astis, 2021; Métrich et al., 2021; Pistolesi et al., 2011; Ripepe et al., 2008; Rosi et al., 2013). Besides, as evidenced by their greater intensity and lower recurrence time, both paroxysms and major explosions are suggested to be fed by deeper, volatile-richer magma (Bertagnini et al., 2011; Bevilacqua et al., 2020; Métrich et al., 2021; Voloschina et al., 2023). The differences between ordinary and non-ordinary explosive activity are related to the activation of distinct magmatic sources: the regular Strombolian activity is fed by volatile-poor, crystal-rich and high-viscosity, high porphyritic (HP) magma stored at shallow (<3 km) levels, and typically ejected as black scoriae (Francalanci et al., 1999; Métrich et al., 2001; Pioli et al., 2014); while major and paroxysmal explosions erupt “golden” pumices associated with a gas-richer, crystal-poor and low-viscosity, low porphyritic magma (LP), that rapidly ascends from a reservoir at depth of ~6–9 km (Aiuppa et al., 2021; Métrich et al., 2010; Voloschina et al., 2023). One of the last non-ordinary periods that produced both explosive and effusive activity, occurred in July–August 2019, when two paroxysms hit the island, causing a fatality, producing pyroclastic flows triggering small tsunamis, originating a two-month-long effusion sourced from summit craters (Aiuppa et al., 2021; Giordano & De Astis, 2021; Laiolo et al., 2022; Ripepe, Lacanna, et al., 2021).

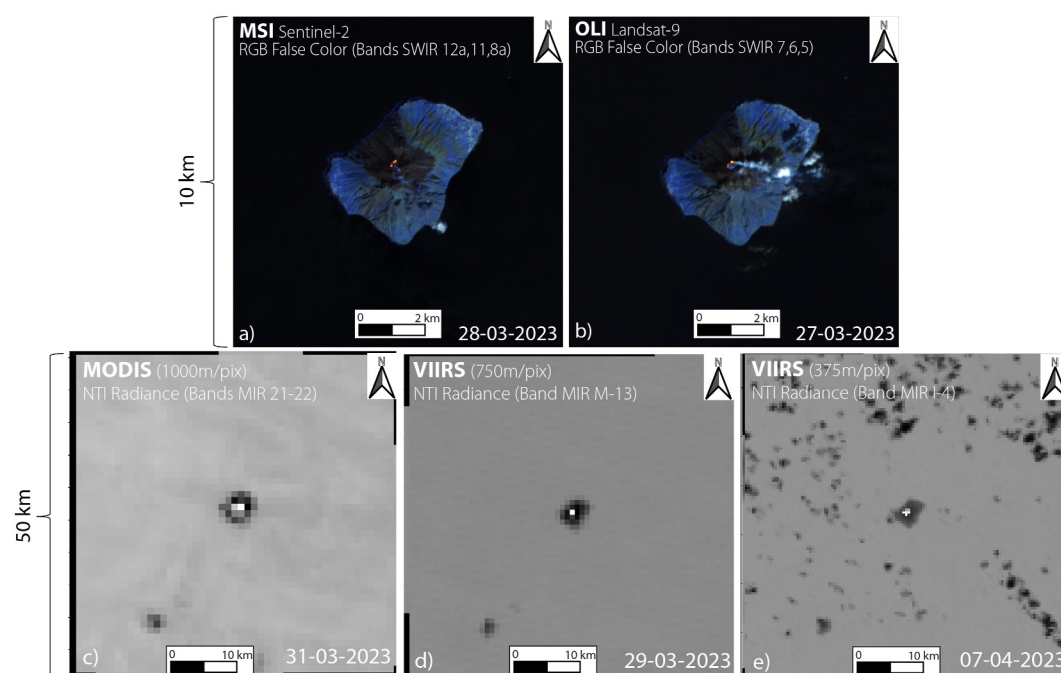
## 2.2. Stromboli's Active Craters

Strombolian activity occurs from a variable number of vents concentrated within the crater terrace (Rosi et al., 2013; Figures 1a and 1b). Location and number of active vents in the crater terrace have continuously changed over time (Calvari et al., 2014; Civico et al., 2021; Marsella et al., 2012). Regular activity results in both constructive and destructive processes, building and disrupting cinder cones and hornitos. Besides, periods of intense activity led to neat growth of the crater terrace due to the increased deposition of eruptive products and overlapping with intra-crater lavas. High energetic explosions and lateral dyke intrusions can instead destabilize and induce partial collapses of the whole crater terrace (up to hundreds of meters deep), as occurred during effusive crises in 2002–2003 and 2007 (see Rosi et al., 2013).

Nonetheless, historical studies demonstrate an extraordinary persistence of the location of the active areas during the past centuries, despite the numerous collapses and regrowth phases of the terrace: Washington (1917) noted that the location of three to six vents had not changed substantially between 1768 and 1915. This vent configuration described more than one century ago, has proven to be recognizable later, remaining mostly unchanged until today (Rittmann, 1931; Rosi et al., 2013). More recently, several authors grouped distinct clusters of active vents (Harris & Ripepe, 2007; Ripepe et al., 2005; Salvatore et al., 2018; Zanon et al., 2009), into three main craters named South West (SW), Central (C) and North East (NE) craters (Gaudin et al., 2017; Harris & Ripepe, 2007; Patrick et al., 2007; Rosi et al., 2013; Figure 1). These three craters, sometimes called crater sectors or crater areas, are aligned along a NE–SW elongated trend, which is ascribed to the presence of a branched feeding dike (or conduit), rising through the edifice up to depths of a few hundred meters (Landi et al., 2011; Ripepe et al., 2008; Rosi et al., 2013; Tibaldi et al., 2008). Geophysical investigations show that the craters are possibly linked at shallow levels to a common source where very-long-period (VLP) seismic events originate (<600 m below crater terrace; Harris et al., 1996; Landi et al., 2011; Ripepe et al., 2005; Ripepe, Delle Donne, et al., 2021; Sugimura et al., 2021).

The activity typically sourced by the three craters is also different; puffing activity (short gas bursts associated with small infrasonic pulses), representing the expression of magmatic continuous degassing, is typically present at one vent at once and predominantly at the C crater; short and frequent explosions, ballistic-dominated and prone to higher infrasonic amplitudes, are associated with NE crater, while long ash-rich bursts are generally produced from the SW crater (Marchetti & Ripepe, 2005; Patrick et al., 2007; Ripepe & Marchetti, 2002). The number of active vents at all craters and the intensity of Strombolian explosive activity is thought to be related to the magma level and the gas flux within the conduit (Calvari et al., 2012; Civico et al., 2021; Ripepe et al., 2008; Spampinato et al., 2008). The rise of magma level in the shallow feeding conduit produces an upward migration of the VLP sources (Marchetti & Ripepe, 2005; Ripepe, Lacanna, et al., 2021), inflation of the summit craters (Di Traglia, Nolesini, et al., 2018), increase in the number of explosions (Calvari et al., 2010; Valade et al., 2016), tremor amplitude (Ripepe et al., 2009), gas flux (Burton et al., 2007; Delle Donne et al., 2022), and in the heat flux detected from satellites (Coppola et al., 2012; Marotta et al., 2015).

Analysis of the thermal amplitude of explosions from ground-based IR cameras demonstrates that the main contribution to the radiated thermal energy is due to the erupted mass composed of ash and bombs (Delle Donne & Ripepe, 2012; Ripepe et al., 2005). However, when measured from space, the heat flux associated with the



**Figure 2.** Sensors of the IR data set utilized in this work. (a) MSI SENTINEL-2 SWIR; (b) OLI LANDSAT-8 & -9 SWIR; (c) MODIS NTI MIR (750 m/pixel); (d–e) VIIRS NTI MIR (750 and 375 m/pixel).

ordinary activity of Stromboli is associated with two main components (Coppola et al., 2012): (a) the number, area, and temperature of the active vents, and (b) the extent and temperature of the deposits present on the crater terrace. Long-term, thermal satellite-based studies reveal the occurrence of fluctuations of the magma level inside the conduit, eventually related to episodes of sustained spattering, fountaining, and outflows, as shown by Coppola et al. (2012). It has been recognized that ordinary activity within the crater terrace produces a radiant heat flux generally up to 30–50 MW. This threshold is exceeded only during periods of lava overflows causing the outpouring of lava from the crater terrace, and marking the transition from the Strombolian to the effusive regime (Coppola et al., 2012, 2014). Given the moderate resolution of sensors used in these past studies, the measured heat fluxes represent the bulk activity of all the thermal sources. Resolving the thermal output from individual craters is the aim of the present work.

### 3. Methodology and Data Set

#### 3.1. Satellite, Sensors, and Metrics

To estimate the heat flux radiated by each crater we used a combination of InfraRed satellite sensors with diverse spectral, spatial, and temporal resolutions (Figure 2). These are the Moderate Resolution Imaging Spectroradiometer (MODIS) and Visible Infrared Imaging Radiometer Suite (VIIRS) for MIR, and the Multi Sensor Instrument onboard SENTINEL-2, and Operational Land Instrument onboard LANDSAT-8 & -9 for SWIR (hereafter named MSI-S2, OLI-L8, and -L9, respectively). The features of sensors and their acquisitions, the processing techniques, and the metrics used to quantify the thermal anomalies are listed in Table 1.

The ability to quantify the heat flux at active volcanoes by MIR-derived data is well established through the estimation of the VRP (Volcanic Radiative Power, in Watt; see next section). In particular, the MIR channel has proven to be extremely robust in measuring the radiative flux produced by Stromboli's thermal activity (Calvari et al., 2010, 2022; Coppola et al., 2012; Ganci et al., 2011; Laiolo et al., 2023; Mattia et al., 2021; Worden et al., 2014; Zakšek et al., 2015). MIR sensors (i.e., MODIS and VIIRS), featuring coarser spatial resolution, high-gain channels to avoid saturation issues and long-time availability, have allowed quantifying of thermal emissions at Stromboli for more than 20 years (Coppola et al., 2023; Wright et al., 2015), providing a solid baseline to interpret thermal signals and representing a reference for satellite-based thermal investigation at active volcanoes (Coppola et al., 2014).

**Table 1**

*Features of Middle InfraRed and Short Wave InfraRed Sensors and Satellites (From Campus et al., 2022; Coppola et al., 2016; Massimetti et al., 2020; Ramsey & Harris, 2013; Wright et al., 2002)*

Sensors	Satellites	Starting acquisition (year)	Wavelengths (μm)	Pixel resolution (m)	Revisit frequency	IR algorithm	Metrics
MODIS	Terra/Aqua	1999/2002	3.96 (MIR)	1,000	~4 images/day	MIROVA (Coppola et al., 2016)	VRP (Watt)
VIIRS	Npp/Noaa20	Jan 2012/Jan 2018	3.74–4.05 (MIR)	375–750	~4 images/day	MIROVA (Campus et al., 2022)	VRP (Watt)
OLI	Landsat-8 & -9	Feb 2013/Nov 2021	0.8–1.6–2.2 (SWIR)	30	~8 days	TI SWIR-MIR (Massimetti et al., 2020)	TI (adim)
MSI	Sentinel-2 (2A & 2B)	Jun 2015/Mar 2017	0.8–1.6–2.2 (SWIR)	20	~5 days	TI SWIR-MIR (Massimetti et al., 2020)	TI (adim)

In contrast, calculating heat flux with SWIR by MSI and OLI high-resolution sensors presents strong limitations, because a smaller pixel's field of view and a greater proportion of any hot surface make SWIR data prone to saturate radiometric parameters at high temperatures (ca. 300°C at 2.2 μm for OLI-L8 and MSI-S2; Hu et al., 2021; Morfitt et al., 2015). SWIR thermal anomalies are generally expressed in terms of total spectral radiance (Genzano et al., 2020; Layana et al., 2020), or in number of alerted pixels (Massimetti et al., 2020; Valade et al., 2019) since other methods to quantify thermal metrics are limited by saturation (Blackett, 2017; Blackett & Wooster, 2011) or sensitive to inter-channel spatial misregistration effects that may impact multi-spectral retrieval approaches (e.g., Fisher & Wooster, 2018; Shephard & Kennelly, 2003). Only a few attempts have been made to merge MIR- and SWIR-derived radiative power into single timeseries (Blackett & Wooster, 2011; Genzano et al., 2023; Marchese, Coppola, et al., 2022; Marchese, Genzano, et al., 2022), but there is currently no satellite monitoring system that provides radiant power estimates based on SWIR data. In the next sections, we present a new, multisensory, simple empirical method, which allowed us to derive volcanic radiative power (VRP) from high-resolution SWIR data. This method can track activity and subtle thermal emissions at the crater scale, calibrating the signal to the more robust MIR data set.

### 3.2. Data Filtering

The analysis is focused on the ordinary Strombolian activity that occurred at Stromboli within the crater terrace (and individual craters) between 2013 and 2023. To inter-calibrate the thermal flux derived from the MIR and SWIR data sets, it was therefore necessary to filter both data sets, by excluding all the alerts detected during periods of higher activity. A database was compiled from the reports of INGV and LGS of the University of Florence ([www.ct.ingv.it](http://www.ct.ingv.it); <http://lgs.geo.unifi.it/>; <https://cme.ingv.it/bollettini-e-comunicati>; Laiolo et al., 2023), by considering the dates of occurrence/duration of any non-ordinary events such as lava overflows, major eruptions (episodes of August–November 2014 and July–August 2019), major explosions, and paroxysms (3 July and 28 August 2019). We thus filtered out from both data sets all the satellite acquisitions that occurred within a time window of ±3 days from the effusive-dominated events (overflows and eruptions), and ±1 day from explosive-dominated events (major explosions and paroxysms). These time windows were adopted to avoid thermal contamination outside periods of ordinary Stromboli activity, including some data influenced by potential unreported events that occurred in proximity to those already reported (e.g., overflows), or by data in which the heat flux was still influenced by the cooling of previously emplaced lava flows. Indeed, including non-ordinary activity and its effects on the detection of the thermal signal would make the correlation between MIR and SWIR, explicitly sought for the ordinary Strombolian activity, uneven.

A further filtering step was done on each data set to clean the satellite signal from corrupted acquisitions, false alerts or unfavorable viewing conditions that strongly influence the thermal data:

- MODIS and VIIRS MIR data set has been filtered by (a) keeping out images with unfavorable viewing geometry (Zenith > 40°), that introduce deformation effects of the projected thermal anomalies and strong effects of thermal bleeding between pixels, (b) selecting only nighttime images, and (c) considering only alerts within a maximum distance of 5 km from volcano summit (to exclude fires or anthropogenic heat sources; see Coppola et al., 2020). It is however significant to emphasize that the VRP quantification from MODIS and



VIIRS MIR images represent a data set that is not corrected for the acquisition conditions, but it simply expresses a measurement of the thermal radiation reaching the MIR sensor *as it is*, possibly including clouds and geometry effects (see Coppola et al., 2020).

- A total of 1,391 SENTINEL-2 and LANDSAT-8/-9 SWIR satellite images, both daytime and nighttime acquisitions (the latter only for L8 and L9), have been visually inspected. The purpose was to assess the quality of images and discard possible effects related to thermal halos, diffraction spikes, or blurring effects, that could alter the size and Thermal Index values of the SWIR thermal anomaly analyzed (see Massimetti et al., 2020).
- L8 and L9 images have been geometrically resampled from 30 to 20 m of pixel dimensions in congruence with the MSI S2 images, to make the SWIR data set spatially homogeneous and co-registered (see Supporting Information S1 for details).

Notably, the SWIR sensors onboard the four platforms have different operational periods (Table 1): L8 was launched in February 2013, S2A and S2B in June 2015 and March 2017, respectively, and L9 in November 2021. This means that the sampling rate of SWIR acquisition grows in the period of analysis as the number of images for time unit, possibly inducing bias, apparent thermal variations, or under-sampling until the complete coverage by the three satellites. However, the cumulative and averaged method applied in the calculation of heat fluxes from SWIR images (see Section 3.4), integrates the different revisit frequencies of satellite overpasses and the time intervals between acquisitions, reducing the effects of asynchrony of the SWIR sensors used.

Between 10 April 2013 and 26 June 2023, we selected 2696 MIR-alerted images from a total of 6,772 overpasses (divided in 3599 MODIS and 3713 VIIRS), and 724 SWIR-alerted images from a total of 1,319 acquisitions (divided in 631 OLI-L8, 96 OLI-L9, and 592 MSI-S2). This results in an alert rate (number of alerts/number of overpasses) of 39% and 54% for MIR and SWIR data sets, respectively. The two data sets clearly outline the strong differences in revisit frequencies of the satellites, with one MIR alert every ca. 1.3 days, and one SWIR alert every ca. 5.1 days.

### 3.3. Calculation of $VRP_{MIR}$

The MODIS and VIIRS data sets have been elaborated using the MIROVA algorithm (Campus et al., 2022; Coppola et al., 2016) which is based on MIR radiance analysis (Table 1), and estimation of the Volcanic Radiative Power ( $VRP_{MIR}$ , in Watt) sourced by high-temperature volcanic features. The combination of the two MIR data sets (MODIS and VIIRS) has been already successfully applied in studying thermal activity in various volcanic settings (Aveni et al., 2023; Campus et al., 2022; Coppola et al., 2022; Reiss et al., 2023).  $VRP_{MIR}$  is calculated by using the MIR method (Wooster et al., 2003) according to which:

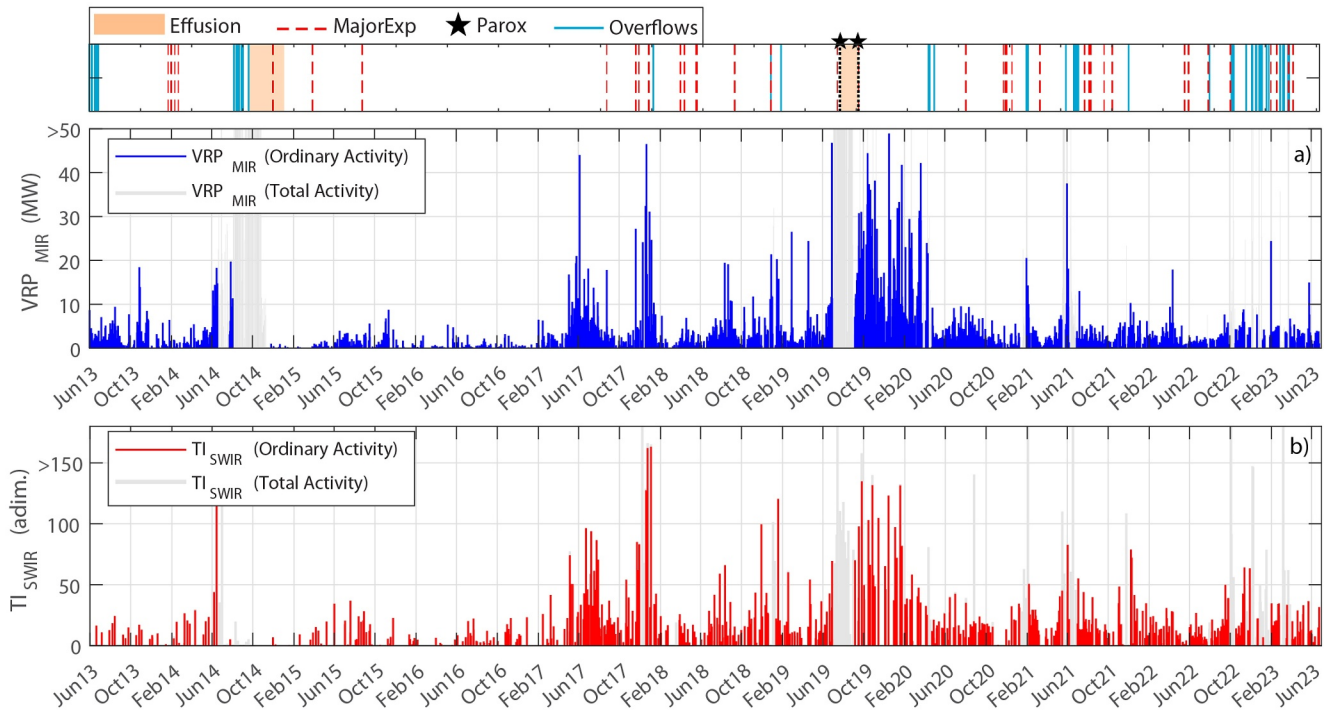
$$VRP_{MIR} = k_{MIR} \times A_{PIX} \times \sum_{i=1}^{i=npix} \Delta L_{MIR(i)} \quad (1)$$

where  $A_{PIX}$  is the pixel size of MODIS or VIIRS MIR images respectively,  $npix$  is the number of alerted pixels, and  $\Delta L_{MIR(i)}$  is the excess of MIR radiance, above the background, of the  $i$ th alerted pixel. The coefficient  $k_{MIR}$  is a wavelength-dependent constant that allows the conversion between MIR radiance and radiative power (see Aveni et al., 2023 for details). This method estimates the radiant power with an error of  $\pm 30\%$ , provided that the temperature of the hot emitter is between 600 and 1600 K (Coppola et al., 2016; Wooster et al., 2003). This error affects the estimates of  $VRP_{MIR}$  for both heat flux measurements by MODIS and VIIRS, although the coefficients used in Equation 1 could vary according to the sensor (Aveni et al., 2023; Campus et al., 2022). Despite the  $\pm 30\%$  error, the  $VRP_{MIR}$  data proved to be extremely valid in estimating the heat flux of volcanic sources having an effective radiating temperature higher than 600 K, or in other terms a fraction of the VTF associated with high-temperature components (Coppola et al., 2023). This is particularly true at Stromboli, a condition that is fully satisfied during Strombolian activity (see Laiolo et al., 2022 about conversion of  $VRP_{MIR}$  heat fluxes in magma output rates), and more precisely for the active vents and for the hot materials erupted by Strombolian explosions in the minutes/hours preceding a satellite acquisition (see Coppola et al., 2016, 2023).

### 3.4. Calculation of $VRP_{SWIR}$

MSI and OLI images are processed analyzing the SWIR-NIR TOA (Top of Atmosphere) reflectance in 3 channels: the  $\rho_{12}$  (2.19  $\mu\text{m}$ ),  $\rho_{11}$  (1.61  $\mu\text{m}$ ), and  $\rho_{8A}$  (0.86  $\mu\text{m}$ ) bands for the MSI-S2 and the  $\rho_7$  (2.11–2.29  $\mu\text{m}$ ),





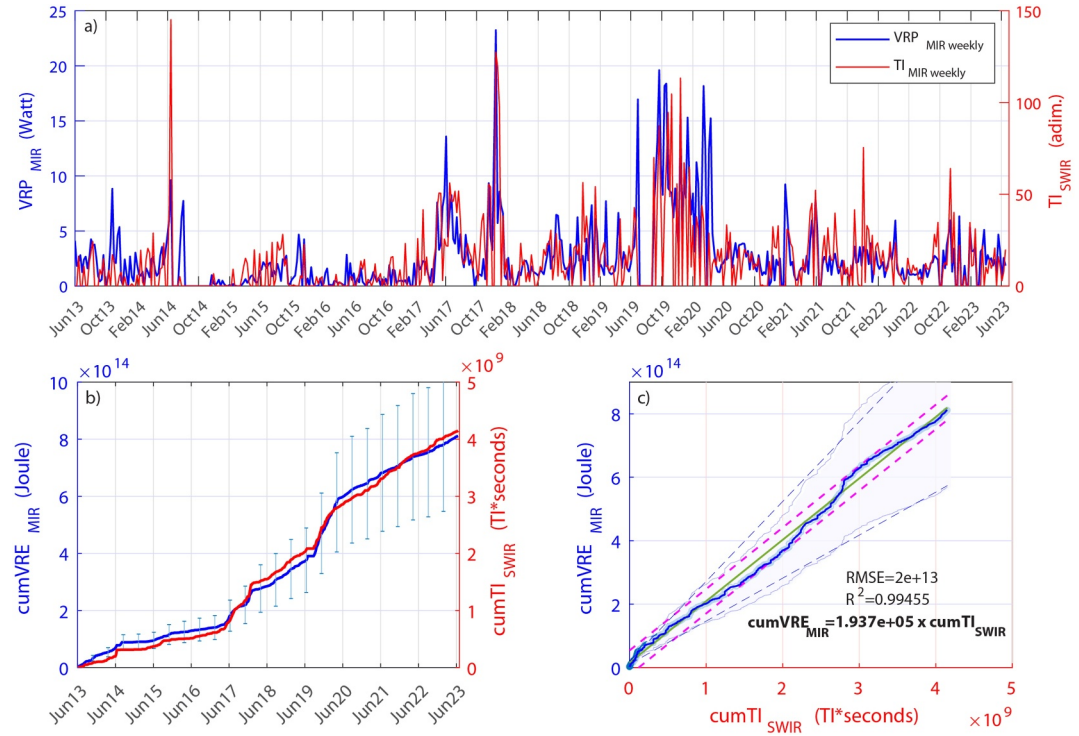
**Figure 3.**  $VRP_{MIR}$  (a) and  $TI_{SWIR}$  from crater terrace (b) timeseries at Stromboli. The code bars above indicates eruption (in orange), major explosions (red dotted bars), overflows events (blue bars) and paroxysms (black stars). The gray bars in each graph represent the  $VRP_{MIR}$  and  $TI_{SWIR}$  without filtering for non-ordinary events, referred as the total Stromboli activity. Consider for the  $VRP_{MIR}$  (panel a) an error of  $\pm 30\%$ , not plotted for graphical reasons (see Figure S1 in Supporting Information S1).

$\rho_6$  (1.57–1.65  $\mu\text{m}$ ), and  $\rho_5$  (0.85–0.88  $\mu\text{m}$ ) bands for the OLI-L8 and OLI-L9. We apply the hybrid hotspot detection algorithm proposed by Massimetti et al. (2020), which is based on fixed ratios and contextual statistical analysis of TOA reflectance. The algorithm detects the number of “hot” pixels and measures the hot area (in  $\text{m}^2$ ) exposed (with an averaged alert false detection rate of 4%). Considering only the hot pixels recognized by the algorithm, we define the Thermal Index ( $TI_{SWIR}$ ) as:

$$TI_{SWIR} = \sum_{i=1}^{i=npix} \rho_{SWIR2}^i + \rho_{SWIR1}^i + \rho_{NIR}^i \quad (2)$$

where  $\rho_{band}^i$  is the reflectance of the  $i^{\text{th}}$  hotspot-contaminated pixel in the three bands of interest (SWIR2:  $\sim 2.2 \mu\text{m}$ , SWIR1:  $\sim 1.6 \mu\text{m}$  and NIR:  $\sim 0.8 \mu\text{m}$ ), and  $npix$  is the total number of hot pixels. The  $TI_{SWIR}$  is therefore an empirical index representative of the bulk thermal anomaly of a VTF and not just of the single pixel. The  $TI_{SWIR}$  is affected by the area of the VTF (embedded in  $npix$ ) and by the temperature of the thermal anomaly, somehow embedded in the TOA  $\rho$  reflectance (the latter being related to spectral radiances; Harris et al., 2013; Massimetti et al., 2020). Unlike  $VRP_{MIR}$ , we cannot calculate a percentage error for  $TI_{SWIR}$  calculation, as it is a direct parameter derived from the sum of reflectances (adimensional) of pixels flagged as hot (or less) by the algorithm of Massimetti et al., 2020. Also, the Thermal Index is an empirical and adimensional parameter, that has been successfully used to study thermal emissions and spatial variations in VTFs in diverse volcanoes (Laiolo et al., 2019; Reiss et al., 2023; Shevchenko et al., 2021).

The  $TI_{SWIR}$  recorded at Stromboli in 2013–2023 is compared with the  $VRP_{MIR}$  timeseries in Figure 3. The two parameters show long-term coherent variations through time and an overall good correlation, confirming  $TI_{SWIR}$  as a proxy for the radiant power of a VTF. Both parameters show lower amplitude and discontinuous thermal emissions between April 2013 and the middle of 2017, while emissions become more consistent and continuous since April 2017, with an increase in magnitude and alert density (Figure 3). Importantly, the similar trends depicted by the two parameters indicate that the different revisit frequency of SWIR images does not affect the detection and the general trend of the VTFs of Stromboli.



**Figure 4.** (a) Timeseries of  $VRP_{MIR}$  weekly in blue and  $TI_{SWIR}$  weekly in red from Stromboli crater terrace ordinary activity; (b) cumulative Volcanic Radiative Energy (Joules) from MODIS MIR (weekly avg.) in blue, with blue bars indicating the error of  $\pm 30\%$ , and cumulative Thermal Index SWIR (weekly avg.) in red; (c) Linear fitting  $k_{swir}$  (solid green line) of  $cumVRE_{MIR}$  versus  $cumTI_{SWIR}$  (magenta dashed lines indicate the 95% prediction interval); the blue pale field represents the error of  $\pm 30\%$  calculated over  $cumVRE_{MIR}$ , with the two blue dashed lines indicating the  $k_{swir} \pm 30\%$ .

According to this qualitative observation, it is possible to state that there is a positive correlation between the  $TI_{SWIR}$  and the  $VRP_{MIR}$ , so that we may write:

$$VRP_{MIR} \propto TI_{SWIR} \quad (3)$$

One of the main issues in looking at the point-by-point relationship between  $VRP_{MIR}$  and  $TI_{SWIR}$  is constituted by the fact that the two families of satellite sensors have different revisit times. The different number of acquisitions of the two data sets is considerable, resulting in periods (from days to months) where several MIR detections are accompanied by few SWIR alerts (see Section 3.2). Thus, correlating single MIR data (i.e.,  $VRP_{MIR}$ ) with each SWIR acquisition (i.e.,  $TI_{SWIR}$ ) is ineffective and meaningless, considering such revisit frequency discrepancies. Additionally, a single  $VRP_{MIR}$  data can be affected by cloudiness and acquisition geometry effects, partially altering the heat flux value measured at the sensor. For these reasons, to quantify the relationship between MIR and SWIR and assess its robustness, minimizing the effects of acquisition conditions, we compute the weekly averages of  $VRP_{MIR}$  and  $TI_{SWIR}$  (Figure 4a) and we integrate these values over consecutive time windows of 1 week to obtain cumulative weekly values (Figure 4b), as follows:

$$cumVRE_{MIR}(i) = \sum_{i=1}^{i=week} \overline{VRP_{MIR}}(i) \times \Delta t \quad (4)$$

$$cumTI_{SWIR}(i) = \sum_{i=1}^{i=week} \overline{TI_{SWIR}}(i) \times \Delta t \quad (5)$$

where in Equation 4  $cumVRE_{MIR}$  is the cumulative Volcanic Radiative Energy (in Joules; see Coppola et al., 2023) radiated after  $i$  weeks,  $\overline{VRP_{MIR}}$  is the weekly averaged values of  $VRP_{MIR}$ , and  $\Delta t$  are seconds in a

week. Similarly, in Equation 5,  $\text{cumTI}_{\text{SWIR}}$  is the time-integrated Thermal Index (in  $\text{TI} \times \text{seconds}$ ) released after  $i$  weeks and  $\text{TI}_{\text{SWIR}}$  represents the weekly averaged TI values (Figure 4b). The  $\text{cumVRE}_{\text{MIR}}$  represents the energy radiated by the activity in the whole crater terrace, and is expressed in Joules (or  $\text{Watt} \times \text{second}$ ). On the other hand, since the TI is dimensionless, its time integration results in cumulative values expressed in  $\text{TI} \times \text{second}$ . The two parameters are shown in Figure 4b, where the  $\text{cumVRE}_{\text{MIR}}$  and  $\text{cumTI}_{\text{SWIR}}$  cumulative curves exhibit coherent trends throughout 2013 and 2023, reaching final values of  $\sim 8 \times 10^{14}$  J and ca.  $4 \times 10^9$   $\text{TI} \times \text{second}$ , respectively (Figure 4b).

The correlation between  $\text{VRP}_{\text{MIR}}$  and  $\text{TI}_{\text{SWIR}}$  thus becomes much more evident and solid when integrated over time, rather than searched between single data acquisitions, which are strongly affected by differences in timing of sensing, geometry, spatial resolution, as well as radiometric characteristics, among the MIR and SWIR thermal sensors used (see Figure S3 in Supporting Information S1). The integration operation on weekly averaged MIR and SWIR data sets, allows us to minimize influences by outliers. In fact,  $\text{cumVRE}_{\text{MIR}}$  and  $\text{cumTI}_{\text{SWIR}}$  show a strong dependence ( $R^2 = 0.995$ , Figure 4c) which allows us to calculate a best-fit coefficient of proportionality,  $k_{\text{SWIR}}$  (in  $\text{Watt}/\text{TI}$ ), equal to:

$$k_{\text{SWIR}} = \frac{\text{cumVRE}_{\text{MIR}}}{\text{cumTI}_{\text{SWIR}}} = 1.937 \times 10^5 \quad (6)$$

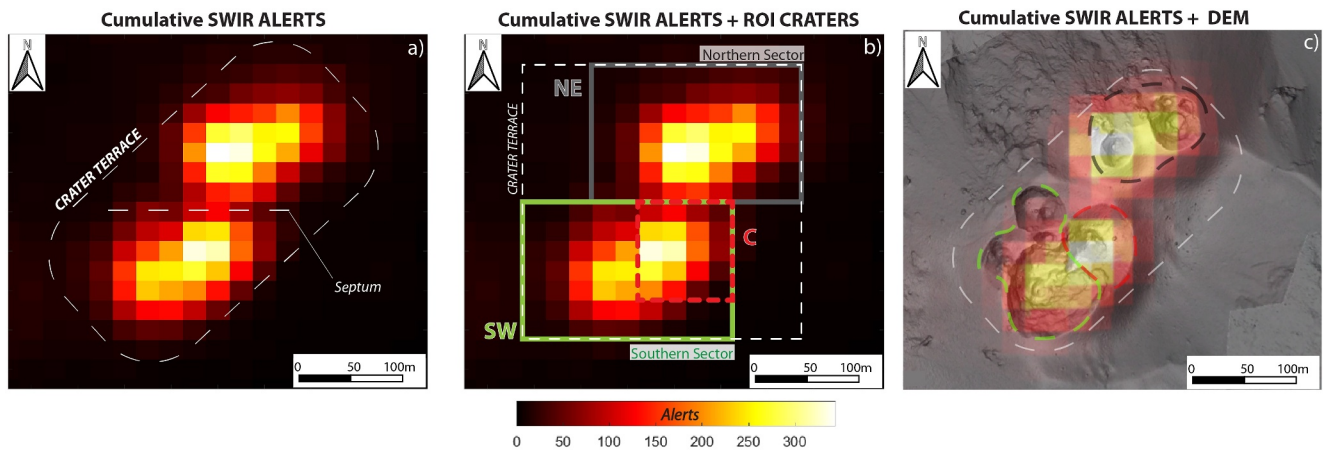
In other words,  $k_{\text{SWIR}}$  is an ad-hoc, best-fit empirical coefficient, calibrated over 10 years of ordinary Strombolian activity, able to describe the relationship between the  $\text{VRP}_{\text{MIR}}$  and the  $\text{TI}_{\text{SWIR}}$ . Accordingly, the volcanic radiant power ( $\text{VRP}_{\text{SWIR}}$ ) can be directly calculated from the  $\text{TI}_{\text{SWIR}}$  measurements over a VTF:

$$\text{VRP}_{\text{SWIR}} = k_{\text{SWIR}} \times \text{TI}_{\text{SWIR}} \quad (7)$$

where  $\text{VRP}_{\text{SWIR}}$  is the heat flux in  $\text{Watt}$  measured by SWIR sensors,  $\text{TI}_{\text{SWIR}}$  is the SWIR reflectances of the VTF (s), and  $k_{\text{SWIR}}$  is the best-fit empirical parameters found by Equation 6 ( $1.937 \times 10^5$   $\text{W}/\text{TI}$  for Strombolian activity). Note that Equation 7 can now be applied pixel by pixel, or on a selected region of interest of a SWIR image, allowing the thermal flux to be calculated for the different craters. Nonetheless, it must be kept in mind that the  $k_{\text{SWIR}}$  value has been calibrated over 10 years of Strombolian activity, and it is suitable for calculating the  $\text{VRP}_{\text{SWIR}}$  associated with this type of activity or VTF. Other types of activities (e.g., lava flows, lava lakes, or lava domes) require an ad-hoc calibration (not treated here), which implicitly takes into consideration the characteristic temperature distribution of the analyzed VTF. In addition, it is crucial to note that  $k_{\text{SWIR}}$ , representing a best-fit linear proportionality between  $\text{cumVRE}_{\text{MIR}}$  and  $\text{cumVRE}_{\text{SWIR}}$ , applies only and exclusively to VTF(s) with pixels of 20 m of spatial resolution (the SWIR data set used in this work), otherwise the number of SWIR hot-spot contaminated pixels would change and the value of  $\text{TI}_{\text{SWIR}}$  accordingly. In case a sensor with a different spatial resolution is used, Equation 7 must be properly corrected by a factor  $f = \text{Apix}/\text{Aref}$ , where  $\text{Apix}$  is the area (in  $\text{m}^2$ ) of the pixel of the SWIR sensor used, and  $\text{Aref}$  is the reference pixel area of  $400 \text{ m}^2$  ( $20 \text{ m} \times 20 \text{ m}$ ; Sentinel-2 or Landsat-8&9 resampled) used in this work. The error of  $\pm 30\%$  of  $\text{VRP}_{\text{MIR}}$  about the quantification of heat flux values propagates through the integration over time to  $\text{cumVRE}_{\text{MIR}}$ , and defines the maximum and minimum error limits for the best-fit coefficient  $k_{\text{SWIR}}$  (Figure 4c).

### 3.5. Definition of Crater Sectors From SWIR Data

The SWIR data sets were used to visualize which sector of the crater terrace was most affected by the presence of thermal anomalies over the 10-year-long analyzed period. We conducted a spatio-temporal analysis on a rectangular region of interest, covering the crater terrace, by stacking all the SWIR images (resampled on a uniform grid with 20 m resolution) with at least one anomaly, thus obtaining a cubic matrix having as many levels as the number of alerted images analyzed. We calculated the number of times each pixel was detected as a hotspot, to produce a cumulative map showing the number of alerts detected during 2013–2023 (Figure 5a). This map represents the temporal persistence of a thermal anomaly in each pixel and highlights the presence of two main clusters of anomalies within the crater terrace, hereby ascribed to *northern* and *southern* crater sector. The two sectors appear similar in size, defining two ellipse-shaped areas measuring approximately  $140 \times 90 \text{ m}$ . They are both oriented approximately  $\text{N } 30^\circ$  and are separated by a cold septum, oriented E-W, characterized by a very low number of thermal anomalies. Inside the northern sector, there is the NE crater, while inside the southern sector,



**Figure 5.** (a) Cumulative Alerts 2013–2023, with limits of crater terrace and cold septum between the two clusters of alerts indicated; (b) definition of the three main ROI craters, North-East, Central and South-West, of the two main crater sectors, Northern and Southern, and of crater terrace limits; (c) Projection of the Cumulative SWIR Alerts 2013–2023 on DEM Stromboli summit map (date July 2022).

there are both the C and the SW crater, as reported in previous works (Calvari et al., 2022; Delle Donne et al., 2022; Salvatore et al., 2018). Based on the historical subdivision into three main craters (cf. Figure 1), we have therefore defined three regions of interest (ROI) that include the three craters, and we have calculated the  $VRP_{SWIR}$  separately for each of them. Accordingly, the sum of the VRP calculated from  $SW_{ROI} + C_{ROI}$  provides a measure of the heat radiated by the entire southern crater sector, while the VRP calculated for the only  $NE_{ROI}$  crater is representative of the heat flux radiated from the northern crater sector.

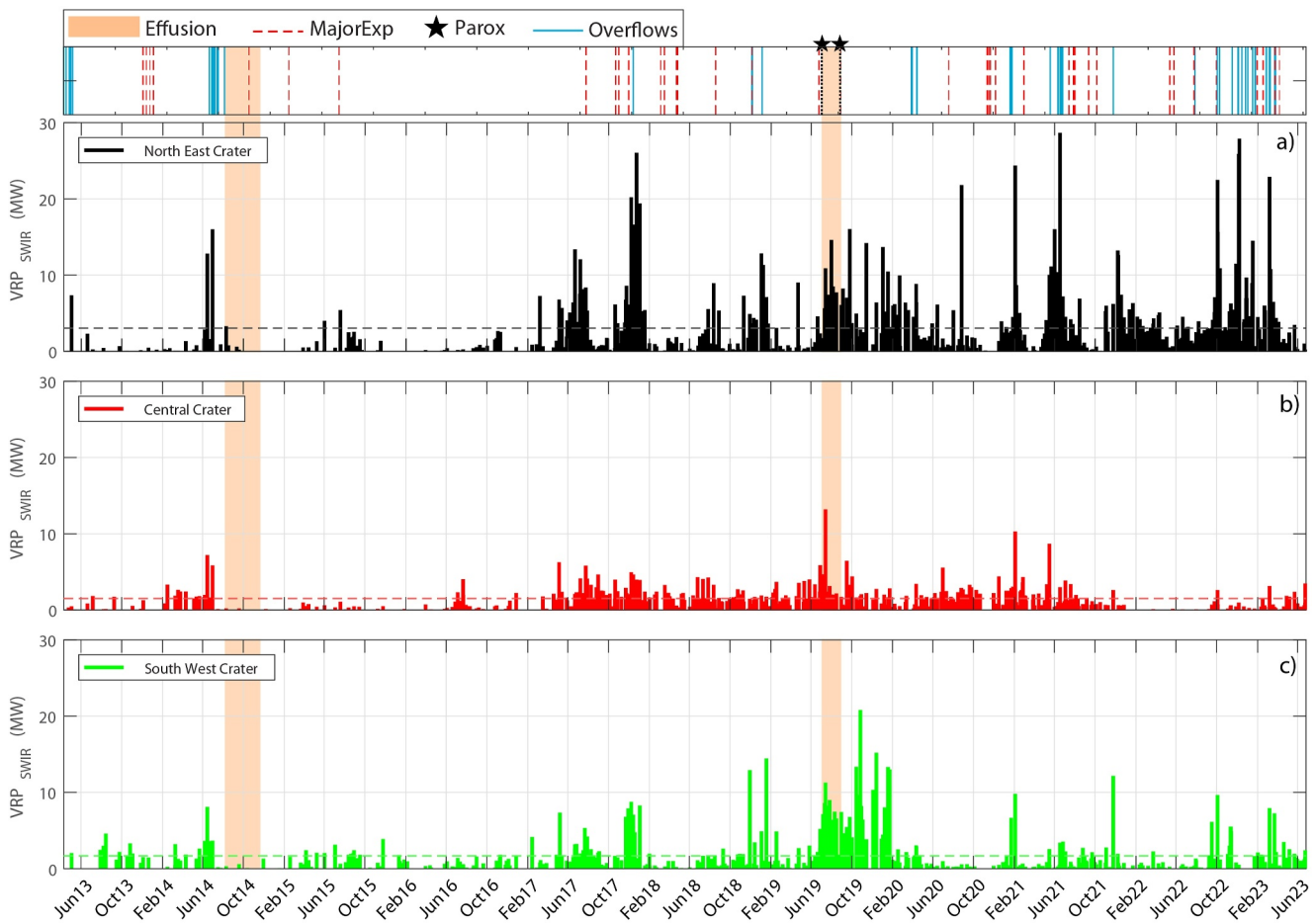
## 4. Results

We present the results derived by the thermal analysis of each crater ROI, to provide (a) the  $VRP_{SWIR}$  timeseries and statistics, differentiated by individual craters and (b) the spatio-temporal evolution of cumulative thermal energy ( $VRE_{SWIR}$ ) released by the single sectors/craters. In this analysis, unlike the calibration stage described in Section 3, we also included the SWIR alerts detected during non-ordinary activity periods, although limiting the analysis only to the spatial elements of ROIs described above. Intra-crater thermal anomalies associated with non-ordinary activity are therefore included while those relating to lava flows along the Sciara del Fuoco are excluded anyway. Importantly, even if  $VRP_{SWIR}$  measurements are presented as unique values and plotted as they are, they present an error of  $\pm 30\%$  on each single point (see Supporting Information S1).

### 4.1. Volcanic Radiative Power of Individual Craters ( $VRP_{SWIR}$ )

Figure 6 shows the  $VRP_{SWIR}$  timeseries of each Stromboli's crater, on a linear scale. The three craters show different characteristics and highlight variability in the space-time distribution of the thermal activity within the crater terrace. The NE crater has the most impulsive nature, with sharp VRP increases, many of which above 10 MW (up to 28 MW in June 2021, Figure 3a). On the contrary, the Central crater shows a lower, more stable thermal emission that, compared to the NE, reflects a more stationary process sustaining the heat flux. The low and steady thermal emissions from the C crater almost disappeared in two periods (after the 2014 eruption and in January–September 2022) during which the crater seemed thermally inactive (Figure 6b). The maximum value (13 MW) was recorded at the end of June 2019, just a few days before the onset of the July 2019 eruption. Finally, the SW crater has a quasi-continuous thermal output, with a marked increase during and following the 2019 eruption (when it reached the peak of 20.8 MW; Figure 6c). The two main effusive periods of 2014 and 2019 are followed by different patterns of  $VRP_{SWIR}$ . After the 2014 flank eruption, the resumption of thermal crater activity was very slow (Figure 6), and started reaching values of  $\sim 5$  MW before at NE (in May 2015), then occurring at C (in August 2016) and later at SW (in first half of 2017). Instead, the 2019 eruption (which did not produce a flank effusion as in 2014) had a different thermal behavior, with the  $VRP_{SWIR}$  values of all craters above the overall average (dashed lines) and high emissions from NE and particularly SW craters, up to  $>20$  MW in the post-eruptive phase.



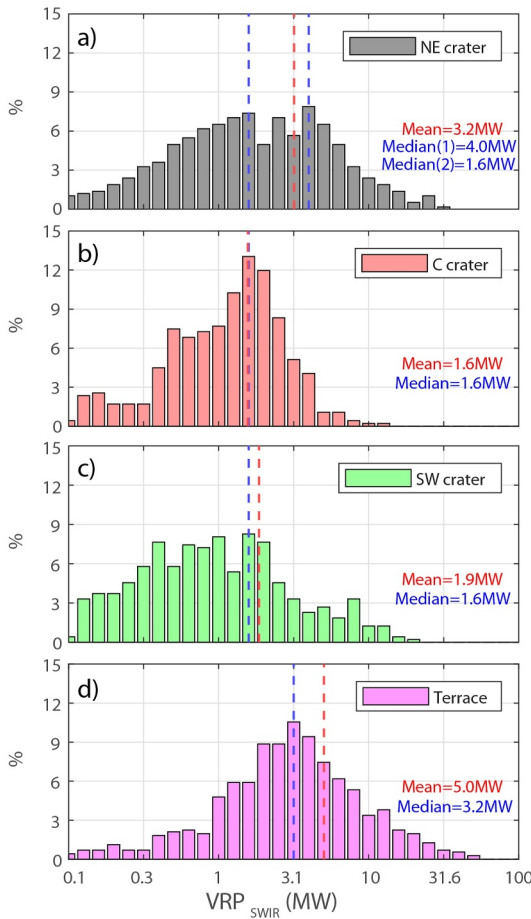


**Figure 6.**  $VRP_{SWIR}$  (MW) from Stromboli craters, (a) North East, (b) Central, and (c) South West. The mean value for each whole crater data set is indicated by colored dotted lines. On the top, with red dotted lines, major explosions; blue bars, overflows, black dotted lines with stars paroxysms, with pale orange field effusive eruptions periods. Consider an error of  $\pm 30\%$  for the  $VRP_{SWIR}$  for all crater sectors (panels a–c) not plotted here for graphical reasons (see Figure S2 in Supporting Information S1).

The statistical distribution of  $VRP_{SWIR}$  observed at the three craters (Figure 7) corroborates their distinct thermal behaviors. The NE crater has a wide distribution of  $VRP_{SWIR}$  values starting from very low ( $VRP_{SWIR} < 0.5$  MW) and several detections between 1 and 3 MW (Figure 7a). Notably, it is the crater with the highest mean value ( $\sim 3.2$  MW) and a tendency to a bimodal distribution, characterized by two peaks at  $\sim 1.6$  and  $\sim 4$  MW (Figure 7a). The C crater exhibits a clear unimodal distribution, with mean and median values coinciding around 1.6 MW and a distribution decreasing sharply for values above 4 MW (Figure 7b). The SW crater has a wide distribution, slightly shifted toward  $VRP_{SWIR}$  values  $< 1$  MW, with mean and median values very close to 1.9 MW (Figure 7c). The overall distribution of the crater terrace embeds all the three thermal behaviors just described, exhibiting an evident unimodal-like distribution with a mode peak of  $\sim 3.2$  MW (mean value of  $\sim 5.0$  MW) and a decreasing tail toward higher heat fluxes reaching ca. 50 MW as upper limit distribution (Figure 7d). This agrees with independent heat loss estimates that constrain the radiant power of Strombolian activity between 7–23 MW (Harris & Ripepe, 2007). It is worth noting that the 50 MW limit corresponds to the transition from Strombolian to effusive activity as recognized by previous works (Coppola et al., 2014).

#### 4.2. Spatio-Temporal Evolution of Cumulative Thermal Energy ( $VRE_{SWIR}$ )

The time integration of the weekly average  $VRP_{SWIR}$  timeseries allowed us to calculate the cumulative energy ( $VRE_{SWIR}$  in Joules) released by each sector/crater through Equation 4. In Figure 8 the cumulative  $VRE_{SWIR}$  is represented for the whole crater terrace, for the two main sectors (Figure 8a) and for the three distinct craters (Figure 8b). The total energy emitted in almost 10 years of activity by the whole crater terrace is about



**Figure 7.** Histogram VRP<sub>SWIR</sub> diagrams in logarithmic scale for each crater and the whole terrace (a, b, c, d), with mean and median values in red and blue, respectively.

$\sim 11.3 \times 10^{14}$  J, which is almost equally partitioned between the northern ( $\sim 5.6 \times 10^{14}$  J) and southern ( $\sim 5.4 \times 10^{14}$  J) sectors. The NE crater radiated most of the energy, followed by the SW crater ( $\sim 3.0 \times 10^{14}$  J) and the C crater ( $\sim 2.3 \times 10^{14}$  J). These values are therefore indicative of time-averaged VRP<sub>SWIR</sub> equal to  $\sim 1.7$ ,  $\sim 0.9$  and  $\sim 0.7$  MW, for the NW, SW and C craters, respectively.

A clear increase in the energy radiated from the entire crater terrace is visible starting from April 2017 with the VRP<sub>SWIR</sub> (weekly time-averaged) of the crater terrace increasing from  $\sim 1.27$  to  $\sim 4.97$  MW (in VRE<sub>SWIR</sub>  $7.6 \times 10^{11}$  J/week to  $3.7 \times 10^{12}$  J/week). This increase is somehow visible in both sectors (Figure 8a), and in all three craters (Figure 8b), albeit with different modalities and intensities.

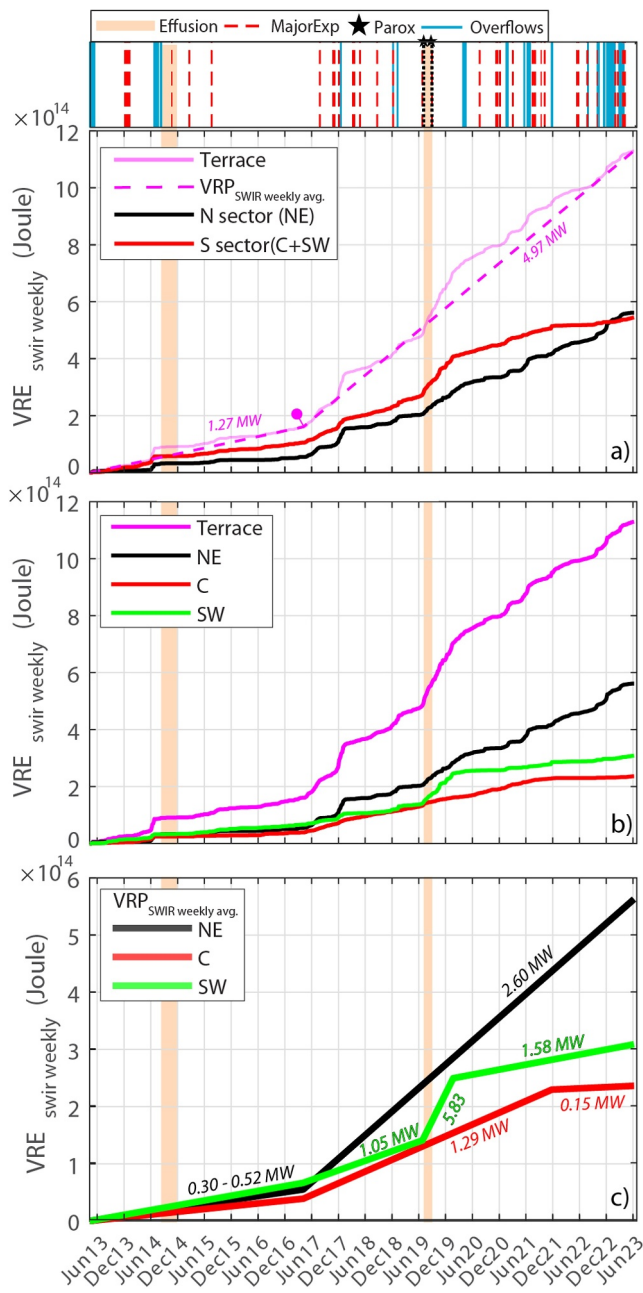
The variable partitioning of the energy released between the individual craters is visible in Figure 9 where the cumulative maps, integrated over 6-month periods, are reproduced. In these maps, the energy released in 6 months is expressed in a hot color bar, so that darkish red tonalities represent low VRE<sub>SWIR</sub> values, while yellowish and brighter tones mean higher VRE<sub>SWIR</sub> (up to  $4 \times 10^{12}$  J of the color scale). Remarkably, until March 2017, a phase of lower thermal emission from all craters is visible, except for the April–September 2014 period, which included the 2014 eruption, when heat flux was influenced by the rise of the magmatic column before the eruption (Valade et al., 2016). Since April 2017, emissions increased and clustered in two to three areas, particularly in the C and NE craters, and more feebly in the SW crater. This pattern changed during the 2019 eruption and later, when emissions were mainly sourced by the SW crater (even beyond the limits defined for the crater terrace; Laiolo et al., 2022; Plank et al., 2019). After the 2019 eruptive period, thermal energies reached a peak sourced by SW crater and by at least two vents in the NE crater (October 2019–March 2020; VRP<sub>SWIR</sub> weekly avg. of 12 MW and a VRE<sub>SWIR</sub> of  $1.5 \times 10^{11}$  J). Thermal outputs generally decreased in the following months, showing a variable thermal source, mainly from NE crater as a major emitter and only a few times by the C and SW craters. This pattern was likely related to phases of sustained Strombolian activity and overflows

occurrence from NE in the first half of 2021 and at the beginning of 2023 (Calvari et al., 2022; <https://www.ct.ingv.it/index.php/monitoraggio-e-sorveglianza/prodotti-del-monitoraggio/comunicati-attivita-vulcanica>, accessed on 20 October 2023).

## 5. Discussion

### 5.1. On the Relation Between VRP<sub>SWIR</sub> and Type of Activity at Individual Craters

The results presented above indicate that each crater has different thermal behavior, as evidenced by the timeseries and frequency distributions of the VRP<sub>SWIR</sub> (Figures 6 and 7). These distinct thermal behaviors are likely linked to shallow eruptive dynamics that manifest through different activity styles characterizing the individual craters. Indeed, the impulsive VRP<sub>SWIR</sub> recorded at the NE crater (Figures 6 and 7), with peaks of ca. 30 MW and the highest VRP<sub>SWIR</sub> among the craters, thermally reflects the typical activity style observed in this sector, with short-lived (<10s), bomb-dominated, highly energetic explosions and with a large amount of scoriae (Marchetti & Ripepe, 2005; Ripepe & Marchetti, 2002). FLIR thermal camera analysis indicates that the NE crater is more prone to ballistic-dominated explosions emplacing coarse-grained material (explosions “type 1,” see Patrick et al., 2007) that generally allow high temperatures to be preserved for longer time than other craters (Marotta et al., 2015). These explosions are accompanied by high gas overpressures and, according to infrasonic data, produce impulsive transient with higher peak amplitude, meaning higher ejected mass (Ripepe et al., 2005). The bimodal distribution VRP<sub>SWIR</sub> (Figure 7a) suggests that periods of sustained Strombolian activity, richer in erupted material and spattering, alternate with periods of lower heat flux, possibly poorer in ejected mass and



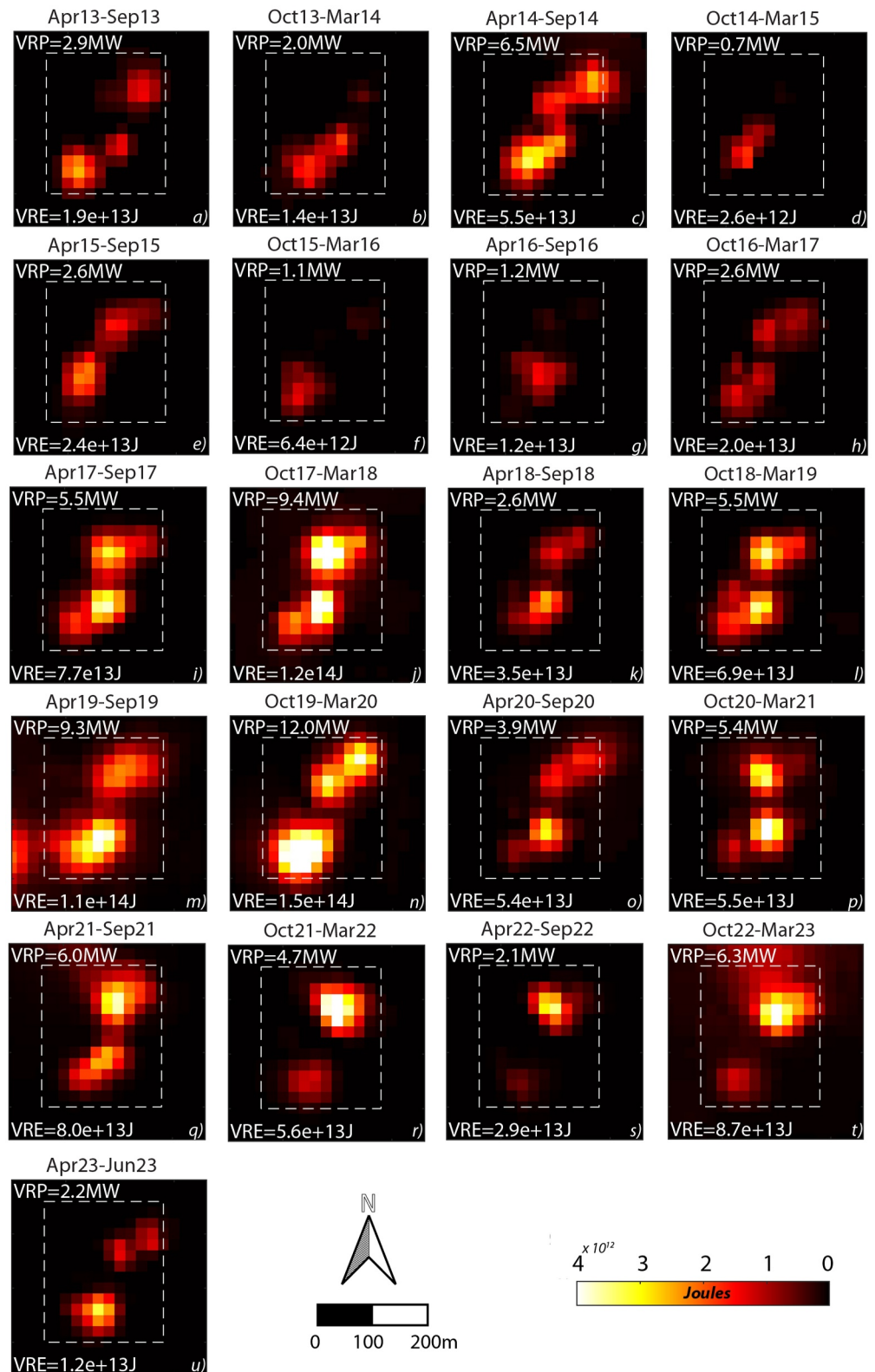
**Figure 8.** (a) Cumulative  $VRE_{SWIR}$  divided for the whole crater terrace (solid magenta line), Northern (solid black line) and Southern (solid red line) sectors; the magenta dashed line, depicts major trend variations in the overall  $VRE_{SWIR}$  crater terrace, with indicated time-averaged weekly  $VRP_{SWIR}$  values for periods before and after April 2017; (b)  $VRE_{SWIR}$  (Joules) at Stromboli sourced from the three craters NE (black line), C (red line) and SW (green line), and from the whole crater terrace (magenta line); (c)  $VRE_{SWIR}$  major trends, with indicated time-averaged weekly  $VRP_{SWIR}$  values (see text for details of the periods). Consider an error of  $\pm 30\%$  for the  $VRE_{SWIR}$ , not plotted here for graphical reasons (see Supporting Information S1) On the top, with red dashed lines, major explosions; blue bars, overflows; black dotted lines with stars, paroxysms; pale orange shaded areas, periods of effusive eruption.

more dominated by degassing. Considering that part of the thermal signal source is represented by the mixture of gas and magmatic fragments ejected by explosions, we can confidently state that  $VRP_{SWIR}$  heat fluxes could represent a combination of these two processes. On the contrary, the C crater exhibits  $VRP_{SWIR}$  lower than other craters, but extraordinarily steady, working as a silent but constant thermal emitter of Strombolian activity. This behavior fits with the observation of continuous degassing, characterized by puffing at stable rates of 30–60 puffs/minute, and infrequent Strombolian explosions (Harris & Ripepe, 2007; Landi et al., 2011; Ripepe et al., 2007). As argued by Ripepe et al. (2008), convection mechanisms and the structure of the shallow system explain why puffing activity is more often stable at the C crater, and only temporarily migrates toward the terrace edges due to a drift of the convection cell centroid. At the SW crater, the  $VRP_{SWIR}$  is spread over a wide range of values, with a longer tail toward low magnitudes and an overall less intense thermal output than NE (Figure 7c). As for NE crater, this evidence could be related to the type of activity generally occurring at SW crater, with longer durations (up to 30s), higher ash contents, barrel-shaped amplitudes of infrasonic signals, thermal signals with complex multiple peaks (Harris & Ripepe, 2007; Ripepe et al., 2005; Schraff et al., 2008). Also, products emitted from the SW vents show colder temperatures (Landi et al., 2011) and lower thermal signals, because the SW crater may be prone to more ash-dominated explosive and typically lower gas overpressures (explosions “type 2,” see Patrick et al., 2007). These data suggest that the  $VRP$  distribution at each crater is somehow linked to the prevalent type of activity and its persistence.

## 5.2. Partitioning and Shifting of Thermal Activity Between Craters

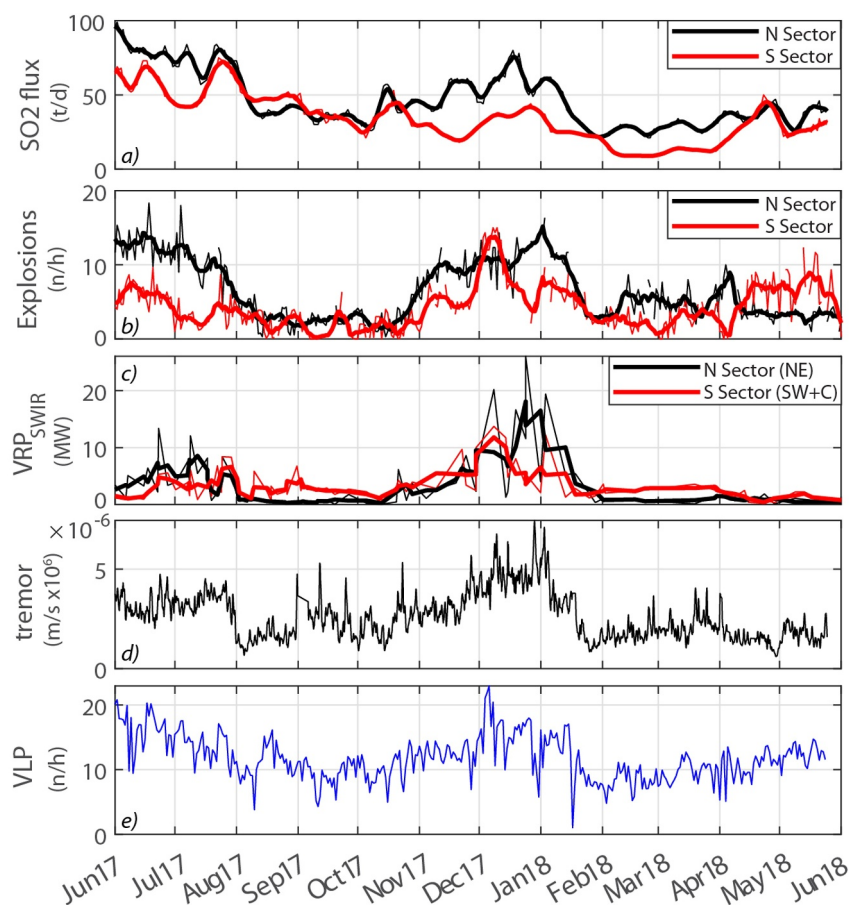
In the short and medium term, the partitioning and shifting of thermal activity between craters is conditioned by the dynamics of the shallow magmatic system. To better characterize the link between thermal flux and surface eruptive dynamics, we compared the  $VRP_{SWIR}$  of individual sectors with other geophysical and geochemical parameters capable of discriminating the source of the activity. In the specific case, we used a limited (from June 2017 to May 2018; Figures 10a–10e) but multi-parametric data set consisting of: (a)  $SO_2$  flux obtained from 2 UV cameras (University of Palermo, Delle Donne et al., 2022), (b) number of explosions, obtained from thermal cameras (INGV; Calvari et al., 2022). To these parameters, we add the tremor amplitude and the number of Very Long Period (VLP) seismic events (University of Firenze), which are key for the comprehension of the overall dynamics of Stromboli activity (Ripepe et al., 2008; Valade et al., 2016). The 2017–2018 analyzed period is a key example of a fluctuating, yet ordinary, Strombolian activity, which occurred approximately three years after the effusive eruption of 2014 and tracked the variations and shifting of the crater’s activity after the gradual resumption of explosions within the crater terrace (Delle Donne et al., 2022).

The  $SO_2$  flux results (Delle Donne et al., 2022) are obtained from two co-exposed UV Cameras, viewing the volcanic plume from two distinct viewing directions. From this, is possible to resolve the relative  $SO_2$  contributions of the NE and SW + C craters to the total  $SO_2$  flux (see Figure 10a), and find that the NE gas contribution increases (relative to the SW + C crater contribution) during phases of escalating Strombolian activity, as indicated



**Figure 9.** (a–u) Stacked  $VRE_{SWIR}$  maps (in Joules) for the Stromboli crater terrace (limits indicated by white rectangle) during time windows of 6 months, from April to September 2013–2023 (last stacking from April to June 2023).  $VRP_{SWIR}$  mean and total  $VRE_{SWIR}$  energy emitted by the crater terrace are reported in each 6 months stacked map.





**Figure 10.** Multi-parametric comparison during June 2017–2018, with (a) SO<sub>2</sub> flux (vent discriminated Southern and Northern craters sector by UV cameras; Delle Donne et al., 2022); (b) Number of explosions from craters by thermal cameras (hourly frequency per day; see Calvari et al., 2022); (c) VRP<sub>SWIR</sub> (vent discriminated crater sectors); (d) tremor amplitude; (e) VLP seismic signal (hourly frequency per day). Gray fields indicate periods of escalation of Strombolian activity. For (a), (b), and (c), solid thick lines are smoothed-Gaussian weekly data, while thin lines are raw data.

by an explosive rate >10 events/hour tracked by thermal cameras (Figure 10b). This trend is perfectly reproduced by tremor amplitude, and to a lesser degree, by the VLP frequency, indicative of the general escalation of Stromboli activity, in two periods: between June–August 2017 and December 2017–January 2018 (gray fields, Figures 10d and 10e). The VRP<sub>SWIR</sub> follows the path indicated by the other parameters, with values exceeding 10 MW during the phase of June–July 2017 and December 2017–January 2018 (the first period less pronounced due to minor revisit time of available satellite images). The partitioning of the activity between northern and southern sectors marked by SO<sub>2</sub> and explosive rate is entirely replicated by the heat flux emissions, with the phases of NE activity escalation well tracked by thermal data, particularly during the winter months between 2017 and 2019.

The general accord in trends of all parameters, and the similar shifting pattern between crater sectors in degassing, explosive rate, and thermal signals, indicate a common process ruling the escalating magnitude of degassing, seismicity, number of explosions and the rise of thermal emissions. These correlations also highlight that the approach presented here can trace the movement of magma/gas at a shallow level in the medium and long term. In fact, the parallel fluctuation of all investigated parameters indicates an evident prominence of the NE sector in recording periods of increased Strombolian activity, being the main promoter and catalyzer, among all craters, of phases of sustained activity from a thermal, explosive, and degassing point of view.

Delle Donne et al. (2022) observed that SO<sub>2</sub> flux from NE crater usually increases to reflect variations in the volcanic activity, as result of an increased gas/magma channeling in the structurally weaker north-eastern portion

of the crater terrace. This is corroborated by thermal observations, highlighting the NE crater as the more reactive to thermal variations in the transition between ordinary and non-ordinary and more explosive activity. In general, the multi-parametric comparison of Figure 10 provides an excellent validation of the thermal fluctuations observed at individual craters and their movement in the crater terrace, providing insights on the spatial and temporal evolution of the thermal regimes. We envisage that future in-depth studies will be able to assess and establish the contribution of magmatic gas and erupted material to the thermal signals recorded by the satellite. At present, the interpretation of the thermal evidence discussed in this work, the latter corroborated by a remarked consistency with ground-based geophysical and geochemical parameters (Figures 6 and 10), supports the hypothesis of a common deeper structure below the multiple active craters (e.g., Giberti et al., 1992; Harris et al., 1996; Ripepe et al., 2005; Rosi et al., 2006), with the central crater hosting most of the degassing, whereas lateral craters being characterized by regular Strombolian explosions with different ash and particles contribution (Landi et al., 2011).

### 5.3. Long-Term Thermal Energy Trends and Pattern

The previous validation confirms that the  $VRP_{SWIR}$  is closely linked to the flux of magma/gas at individual craters and may be used to detect variations in space and time of the shallow magma channeling. The analysis of the cumulative energy curves allows us to highlight peculiar trends for the individual sectors and craters characterizing the eruptive activity between 2013 and 2023 (Figure 8c). We have little data before the 2014 eruption to accurately define trends and patterns, but it is evident that this effusive event was preceded by the rise of the magma column (Valade et al., 2016) and the consequent increase in heat flux at all three craters (Figures 6 and 8). Vice versa, the months that followed the 2014 eruption represent the period of lowest thermal emissions from all craters. This reflects the drastic lowering of the magmatic column resulting from the effusion of over 5 Mm<sup>3</sup> of lava (Ripepe et al., 2017; Valade et al., 2016). The reactivation of the craters seems to have occurred irregularly starting from the NE, then the Central, and then the SW (Figure 6). However, the overall energy radiated from the entire crater terrace shows a clear increase since 2017 (from 1.27 MW to ca. 5 MW), which is reflected in both sectors, as well as in all three craters. This change suggests that at the origin of the increased heat flux there was a common and possibly deeper process, capable of conditioning the surface activity of all the craters. This possibly marks the moment in which the shallow magmatic system, perturbed by the 2014 eruption, recovered ordinary conditions with fluctuating Strombolian activity at the surface causing the detection of frequent thermal anomalies (see previous paragraph).

Starting from April 2017 all three craters exhibit an increase in heat flux, but with different slopes and patterns (Figure 8). The thermal activity at NE crater almost grows by five times its heat flux (from ~0.43 to ~2.60 MW on  $VRP_{SWIR}$  weekly time-averaged, increase of ~505%; Figure 8c). Although minor fluctuations were observed in the medium term (essentially during periods of overflows), this thermal regime remained relatively stable throughout the whole, post-2014 investigated period, and persist until the end of the analysis in 2023. Notably, this steady-state behavior was not disturbed even by the 2019 eruption (Figures 6 and 8c). Similarly, thermal emissions at the C crater see a marked increase since April 2017 with time-averaged  $VRP_{SWIR}$  passing from ~0.30 to ~1.29 MW, increase of ~330%. In the week before the 2019 eruption, the Central crater recorded the highest, although isolated,  $VRP_{SWIR}$  (~13 MW; Figure 6), after which the flux returned to stable values similar to the pre-eruptive period (~0.30 MW). A clear decrease in the thermal activity of this crater is observed starting from November 2021, with the thermal energy becoming very low (~0.15 MW) and comparable to the 2014 post-eruptive period. The SW crater thermal output also shows an increase in April 2017 (from ~0.52 to ~1.05 MW), but less rapid and more modest than at the NE. This suggests that in the SW crater the resumption of activity after the 2014 eruption began later and in a less pronounced way. The SW crater also shows an increase in heat flux in the weeks preceding the 2019 eruption (Figure 6), but differently from the C crater, the activity persisted at higher levels (~5.83 MW), even in the following months. During the eruptive period, the SW crater showed high-energetic Strombolian explosions accompanied by lava flows extending to the southern sector of the Sciara del Fuoco. This was followed by a period of intense spattering activity since September 2019 (Civico et al., 2021; Laiolo et al., 2022; Plank et al., 2019). These thermally energetic processes represent a strong radiative source in the summit area, which is reflected by the highest  $VRP_{SWIR}$  and  $VRE_{SWIR}$  values in the 10 years of analysis of SW crater (Figures 9m and 9n). In contrast with the 2014 flank effusion which drained the magmatic column and partially emptied the shallow reservoir (resulting in absent to very low  $VRP_{SWIR}$  emission from summit craters; Figure 6), the 2019 eruption (started with the third of July paroxysm) evidently represented a different process. In

fact, the 2019 eruption was not accompanied by the collapse of the crater area, but rather by a phase of extremely efficient convecting regime causing high SO<sub>2</sub> emissions and spattering activity (Aiuppa et al., 2021; Laiolo et al., 2022) this, in turn, originating unprecedented thermal emission from craters. This intense post-eruptive phase persisted until early 2020, after which the long-term heat flux of the SW crater returned to stabilize at pre-2019 eruptive values (~1.58 MW).

Thus, the 2019 eruptive crisis represents an unusual eruption, considering that for more than 50 years (after the 1967 eruption) no effusive eruptions (lava volumes > 1 Mm<sup>3</sup>) have been directly sourced by the SW crater nor from the southern sector of the crater terrace (Calvari & Nunnari, 2023; Marsella et al., 2012). Looking at the VRE<sub>SWIR</sub> trends between craters (Figure 8), the 2019 event represented a changing point in the long-term thermal budgets of SW crater. First a sharp increase concurrent with the eruption and following months occurs, and then a reduction in the efficiency of the southern sector to release thermal emission, likely related to a change in the feeding architecture of the branched conduit at shallow level due to the extraordinary cascade of energetic events of summer 2019, considering two paroxysms and an effusive phase lasted two months. On the other hand, the 2019 eruption did not have surprisingly a significant impact on the thermal budget of the northern sector which, instead, has continued to rise almost steadily, except for short-term steps due to overflows and periods of high Strombolian activity (Figure 8b).

Besides the last eruptions, in the last 10 years, the long-term patterns of thermal output are well consistent with Stromboli's recent eruptive behavior. VRP<sub>SWIR</sub> and VRE<sub>SWIR</sub> values indicate a very low thermal level between 2014 and mid-2017 from all craters (Figures 6, 8, and 9), this likely related to a lower magma column and a minor efficiency of shallow feeding system to emit thermal energy (Allard et al., 2008; Coppola et al., 2012; Harris & Stevenson, 1997a; Ripepe et al., 2008). After the 2014 eruption, Stromboli showed very low volcanic activity for two years (Delle Donne et al., 2017; Di Traglia, Calvari, et al., 2018; Valade et al., 2016), and only from 2017 to 2018 gradually Strombolian activity started to increase (Delle Donne et al., 2022). The progressive reactivation of shallow magma transport is also manifested by the occurrence of non-ordinary events, such as the major explosion of 26 July 2017 (after two years of major explosion quiescence), a series of major explosions in October–December 2017 producing voluminous spatter production (Di Stefano et al., 2020), and the occurrence of short-lived summit overflows that took place on 15 Dec 2017, these fed by the NE crater sector (Figure 8; Delle Donne et al., 2022; Giudicepietro et al., 2019). On a general view, a new higher energetic stage started in mid-2017 and the increase in thermal output by the crater terrace is closely related to this resumption. It's worth noting that recent petrochemical findings (clinopyroxene antecryst analysis of erupted materials during the latter decades) suggest a rejuvenation process of the shallow reservoir of Stromboli between 2003 and 2017, with a mafic magma recharge event in late 2017 (Di Stefano et al., 2020; Petrone et al., 2022), in line with the thermal evidence of a renewed Stromboli activity from craters in the same period.

Remarkably, within the investigated period, the two crater sectors radiate almost the same amount of energy (approx.  $5.5 \times 10^{14}$  J each), although over time the balance oscillates in favor of one sector or the other. This balanced partitioning suggests that the shifting from one sector to another reflects rather superficial dynamics that tend to keep the long-term evolution (growth and destruction) of the crater terrace balanced. This is also corroborated by the fact that over the decades or centuries, the crater terrace has always evolved (almost) symmetrically, without evident imbalances in the growth/collapse of one sector rather than another. On the other hand, the 2019 eruption possibly defines the most recent changing point for the energy release from crater sectors. Starting from 2020 there is a clear decoupling of trends, which sees the northern sector being much more energetic than the southern one. This discrepancy is reflected in the large number of overflows that occurred during this period, all associated with NE crater thermal activity.

## 6. Conclusions

We presented 10 years of thermal satellite-based analysis of the volcanic activity of Stromboli sourced by active craters, with an unprecedented level of details, both spatially and temporally, taking advantage of a multi-sensor and multi-spatial space-based approach. We explored the relationship between the Volcanic Radiative Power (in Watt) and the Thermal Index (TI), and the related Volcanic Radiative Energy (in Joules), measured by MIR (MODIS & VIIRS) and SWIR (MSI SENTINEL-2 & OLI LANDSAT-8/9) sensors during ordinary activity. Through this relationship, for the first time, we quantitatively measured the heat flux (VRP<sub>SWIR</sub>) and thermal energy (VRE<sub>SWIR</sub>) produced by the Stromboli crater terrace and single crater sectors in the last 10 years of

activity. Using the spatial resolution offered by the SWIR sensors we constrained the thermal signature of each crater on a multiyear scale of analysis, a goal otherwise impossible to achieve with MODIS-type sensors.

The analysis depicts remarkable differences in the thermal behavior of the three main craters, the North East (impulsive and higher emitter), Central (stable and lower), and South West (highly variable), with  $VRP_{SWIR}$  magnitudes and distribution patterns, confirming the differences in explosive dynamics observed at the craters (ballistic-dominated vs. gas-dominated vs. ash-dominated). The thermal high-resolution investigation revealed short-term variations (months) in the source of thermal emissions between craters, but an extreme long-term (years) stability of the location of the main craters, in agreement with the historically recognized presence at Stromboli of three main craters, along with evidence of two distinct thermal macro sectors in the northern and southern parts of the terrace that characterized the last 10 years of activity, with an almost paired balanced budget of thermal emitted energy. The long-term thermal budget shows a total of  $\sim 12 \times 10^{14}$  J emitted in the last 10 years, while a remarked shift in terms of  $VRE_{SWIR}$  released was observed since April 2017. This was suggested to be related to the progressive reactivation of shallow magma transport and convective regime, feeding Strombolian (and so thermal) activity at the main craters, remarking the beginning of new increase explosivity behavior of the volcano, which is ongoing until today.

Significantly, the results achieved by the analysis of long-term satellite signals, although at a completely different spatial and temporal scale of investigation from ground-based approaches, contribute to improve the conceptual model of the shallow magmatic system of Stromboli volcano. Thermal evidence supports the hypothesis of a deeper link between the multiple craters, with lateral craters more prone to exhibit Strombolian explosions and the NE as more prone to be thermally responsive to volcanic activity variations, tracking better than other craters the transition between ordinary and non-ordinary regime. Thermal emissions, consisting of the joint contribution of active craters in addition to the hot material and gas released, vary in intensity and location accordingly with gas and explosive rates, and this evidence reflects a shared magmatic control on the surface activity. Moreover, even if the thermal emissions show short-term spatio-temporal evolution related to activity variations, the general location and explosive features of the three active craters broadly remain stable within the crater terrace in the last 10 years; this evidence confirms the extreme stability of shallow feeding system, able to recover and rebuilt its original structure and dynamics after major energetic eruptions, such as the 2014 effusion and the paroxysms-effusive 2019 crisis.

The innovative method here proposed represents an important enhancement for the quantification of radiative power of high-temperature (integrated  $T > 600\text{K}$ ) Volcanic Thermal Features, using high spatial resolution SWIR sensors, an otherwise complex goal given the saturation issues of SWIR imagery. The empirical best-fit relationship  $k_{swir}$ , deriving from MIR-SWIR comparison, here specifically calibrated for thermal signals of Stromboli ordinary activity, could be theoretically found on other volcanoes with multiple thermally active craters. Indeed, we can expect that  $k_{swir}$  changes as the thermal output of different volcanic activity and the thermal distribution of its VTFs vary. In this view, likely, the  $k_{swir}$  constant (i.e., the ratio between thermal energy emitted in MIR and SWIR) found here could be somewhat similar if studied in other volcanic settings that show Strombolian-type volcanic activity. Nonetheless, we suggest caution in reproducing the method presented here without careful calibration and filtering of the data, especially in more complex temperature distributions of VTFs, where the high-temperature portion, to which MIR and SWIR are very sensitive, may vary rapidly over time (lava flows) or be unstable or minority (lava domes). From this perspective, the approach here presented and its possible results are of great impact and will require further study for larger applicability on other volcanoes.

Finally, the proposed integration of satellite thermal data from various sensors allows repeatable measurements for monitoring Stromboli, and open-vent systems characterized by continuous release of thermal emission. Tracking thermal variations in multi-crater contexts and building knowledge of a thermal reference (i.e., thermal baseline), in combination with geophysical and geochemical parameters, is a precious supplement for monitoring applications and risk reduction purposes, even at-well monitored volcanoes as Stromboli.

### Conflict of Interest

The authors declare no conflicts of interest relevant to this study.



## Data Availability Statement

ESA-Copernicus (<https://dataspace.copernicus.eu/>) publicly provides Sentinel-2 data via the S3 object storage service via Copernicus Data Space Ecosystem (<https://dataspace.copernicus.eu/>). NASA/USGS publicly provides Landsat-8 & -9 data via AWS service (<https://registry.opendata.aws/usgs-landsat>). The data files used in this paper, such as the raw thermal satellite MIR and SWIR data, and the final heat flux  $VRP_{SWIR}$  data set from Stromboli crater sectors, are available at (Massimetti et al., 2024; <https://osf.io/zdbyq/>). MODIS MIR data analyzed by the MIROVA algorithm can be accessed also by the depository at <https://osf.io/zm62w/>. The thermal algorithm used to detect, locate, and measure MIR thermal anomalies in MODIS and VIIRS data sets are published and explained in Coppola et al. (2016, 2023) and in Campus et al. (2022). The thermal algorithm used to detect, locate, and count SWIR thermal anomalies in MSI Sentinel-2 and OLI Landsat-8 & -9 are published and explained in Massimetti et al. (2020).

## Acknowledgments

MIROVA is a collaborative project between the Universities of Turin and Florence (Italy). We acknowledge the LANCE-MODIS data system for providing MODIS and VIIRS Near Real Time products. The study has been developed in the ambience of the service activity enhancement project “Sviluppo del sistema unico (INGV-Università) di monitoraggio vulcanico e rilevamento precoce dei maremoti e delle esplosioni parossistiche di Stromboli” funded by the Dipartimento della Protezione Civile and the INGV. The study does not necessarily reflect the policy and position of the Istituto Nazionale di Geofisica e Vulcanologia and Dipartimento della Protezione Civile, Italy. Open access publishing facilitated by Università degli Studi di Torino, as part of the Wiley - CRUI-CARE agreement.

## References

- Acocella, V., Ripepe, M., Rivalta, E., Peltier, A., Galetto, F., & Joseph, E. (2024). Towards scientific forecasting of magmatic eruptions. *Nature Reviews Earth & Environment*, 5(1), 5–22. <https://doi.org/10.1038/s43017-023-00492-z>
- Aiuppa, A., Bertagnini, A., Métrich, N., Moretti, R., Di Muro, A., Liuzzo, M., & Tamburello, G. (2010). A model of degassing for Stromboli volcano. *Earth and Planetary Science Letters*, 295(1–2), 195–204. <https://doi.org/10.1016/j.epsl.2010.03.040>
- Aiuppa, A., Bitetto, M., Delle Donne, D., La Monica, F., Tamburello, G., Coppola, D., et al. (2021). Volcanic CO<sub>2</sub> tracks the incubation period of basaltic paroxysms. *Science Advances*, 7(38), eabh0191. <https://doi.org/10.1126/sciadv.abh0191>
- Aiuppa, A., de Moor, J. M., Arellano, S., Coppola, D., Francofonte, V., Galle, B., et al. (2018). Tracking formation of a lava lake from ground and space: Masaya volcano (Nicaragua), 2014–2017. *Geochemistry, Geophysics, Geosystems*, 19(2), 496–515. <https://doi.org/10.1002/2017GC007227>
- Allard, P., Aiuppa, A., Burton, M., Caltabiano, T., Federico, C., Salerno, G., & La Spina, A. (2008). Crater gas emissions and the magma feeding system of Stromboli volcano. In S. Calvari, S. Inguaggiato, G. Puglisi, M. Ripepe, & M. Rosi (Eds.), *The Stromboli Volcano: An integrated study of the 2002–2003 eruption, Geophysics Monograph Series* (Vol. 182, pp. 65–80). American Geophysical Union. <https://doi.org/10.1029/182GM07>
- Allard, P., Carbonnelle, J., Métrich, N., Loyer, H., & Zettwoog, P. (1994). Sulphur output and magma degassing budget of Stromboli volcano. *Nature*, 368(6469), 326–330. <https://doi.org/10.1038/368326a0>
- Andronico, D., Cannata, A., Di Grazia, G., & Ferrari, F. (2021). The 1986–2021 paroxysmal episodes at the summit craters of Mt. Etna: Insights into volcano dynamics and hazard. *Earth-Science Reviews*, 220, 103686. <https://doi.org/10.1016/j.earscirev.2021.103686>
- Aveni, S., Laiolo, M., Campus, A., Massimetti, F., & Coppola, D. (2023). The capabilities of FY-3D/MERSI-II sensor to detect and quantify thermal volcanic activity: The 2020–2023 Mount Etna case study. *Remote Sensing*, 15(10), 2528. <https://doi.org/10.3390/rs15102528>
- Barberi, F., Civetta, L., Rosi, M., & Scandone, R. (2009). Chronology of the 2007 eruption of Stromboli and the activity of the Scientific Synthesis Group. *Journal of Volcanology and Geothermal Research*, 182(3–4), 123–130. <https://doi.org/10.1016/j.jvolgeores.2008.09.019>
- Barberi, F., Rosi, M., & Sodi, A. (1993). Volcanic hazard assessment at Stromboli based on review of historical data. *Acta Vulcanologica*, 3, 173–187.
- Barnie, T. D., Oppenheimer, C., & Pagli, C. (2016). Does the lava lake of Erta Ale volcano respond to regional magmatic and tectonic events? An investigation using Earth observation data. In T. J. Wright, A. Ayele, D. J. Ferguson, T. Kidane, & C. Vye-Brown (Eds.), *Magmatic rifting and active volcanism* (Vol. 420(1), pp. 181–208). Geological Society, London, Special Publications. <https://doi.org/10.1144/SP420.15>
- Behncke, B., Branca, S., Corsaro, R. A., De Beni, E., Miraglia, L., & Proietti, P. (2014). The 2011–2012 summit activity of Mount Etna: Birth, growth and products of the new SE crater. *Journal of Volcanology and Geothermal Research*, 270, 10–21. <https://doi.org/10.1016/j.jvolgeores.2013.11.012>
- Bertagnini, A., Di Roberto, A., & Pompilio, M. (2011). Paroxysmal activity at Stromboli: Lessons from the past. *Bulletin of Volcanology*, 73(9), 1229–1243. <https://doi.org/10.1007/s00445-011-0470-3>
- Bevilacqua, A., Bertagnini, A., Pompilio, M., Landi, P., Del Carlo, P., Di Roberto, A., et al. (2020). Major explosions and paroxysms at Stromboli (Italy): A new historical catalog and temporal models of occurrence with uncertainty quantification. *Scientific Reports*, 10(1), 17357. <https://doi.org/10.1038/s41598-020-74301-8>
- Blackett, M. (2017). An overview of infrared remote sensing of volcanic activity. *Journal of Imaging*, 3(2), 13. <https://doi.org/10.3390/jimaging3020013>
- Blackett, M., & Wooster, M. J. (2011). Evaluation of SWIR-based methods for quantifying active volcano radiant emissions using NASA EOS-ASTER data. *Geomatics, Natural Hazards and Risk*, 2(1), 51–78. <https://doi.org/10.1080/19475705.2010.541501>
- Burton, M. R., Mader, H. M., & Polacci, M. (2007). The role of gas percolation in quiescent degassing of persistently active basaltic volcanoes. *Earth and Planetary Science Letters*, 264(1), 46–60. <https://doi.org/10.1016/j.epsl.2007.08.028>
- Calvari, S., Bonaccorso, A., & Ganci, G. (2021). Anatomy of a Paroxysmal Lava Fountain at Etna Volcano: The case of the 12 March 2021, episode. *Remote Sensing*, 13(15), 3052. <https://doi.org/10.3390/rs13153052>
- Calvari, S., Bonaccorso, A., Madonia, P., Neri, M., Liuzzo, M., Salerno, G., et al. (2014). Major eruptive style changes induced by structural modifications of a shallow conduit system: The 2007–2012 Stromboli case. *Bulletin of Volcanology*, 76(7), 841. <https://doi.org/10.1007/s00445-014-0841-7>
- Calvari, S., Büttner, R., Cristaldi, A., Dellino, P., Giudicepietro, F., Orazi, M., et al. (2012). The 7 September 2008 Vulcanian explosion at Stromboli volcano: Multiparametric characterization of the event and quantification of the ejecta. *Journal of Geophysical Research*, 117(B5), B05201. <https://doi.org/10.1029/2011JB009048>
- Calvari, S., Di Traglia, F., Ganci, G., Bruno, V., Ciancetto, F., Di Lieto, B., et al. (2022). Multi-parametric study of an eruptive phase comprising unrest, major explosions, crater failure, pyroclastic density currents and lava flows: Stromboli volcano, 1 December 2020–30 June 2021. *Frontiers in Earth Science*, 10, 899635. <https://doi.org/10.3389/feart.2022.899635>

- Calvari, S., Giudicepietro, F., Di Traglia, F., Bonaccorso, A., Macedonio, G., & Casagli, N. (2021). Variable magnitude and intensity of Strombolian explosions: Focus on the eruptive processes for a first classification scheme for Stromboli Volcano (Italy). *Remote Sensing*, 13(5), 944. <https://doi.org/10.3390/rs13050944>
- Calvari, S., Lodato, L., Steffke, A., Cristaldi, A., Harris, A. J. L., Spampinato, L., & Boschi, E. (2010). The 2007 Stromboli eruption: Event chronology and effusion rates using thermal infrared data. *Journal of Geophysical Research*, 115(B4), B04201. <https://doi.org/10.1029/2009JB006478>
- Calvari, S., & Nunnari, G. (2023). Statistical insights on the eruptive activity at Stromboli Volcano (Italy) recorded from 1879 to 2023. *Remote Sensing*, 15(19), 4822. <https://doi.org/10.3390/rs15194822>
- Campion, R., & Coppola, D. (2023). Classification of lava lakes based on their heat and SO<sub>2</sub> emission: Implications for their formation and feeding processes. *Frontiers in Earth Science*, 11, 1040199. <https://doi.org/10.3389/feart.2023.1040199>
- Campus, A., Laiolo, M., Massimetti, F., & Coppola, D. (2022). The transition from MODIS to VIIRS for global volcano thermal monitoring. *Sensors*, 22(5), 1713. <https://doi.org/10.3390/s22051713>
- Cannata, A., Sciotto, M., Spampinato, L., & Spina, L. (2011). Insights into explosive activity at closely-spaced eruptive vents using infrasound signals: Example of Mt. Etna 2008 eruption. *Journal of Volcanology and Geothermal Research*, 208(1–2), 1–11. <https://doi.org/10.1016/j.jvolgeores.2011.09.003>
- Chaussard, E., Amelung, F., & Aoki, Y. (2013). Characterization of open and closed volcanic systems in Indonesia and Mexico using InSAR time series. *Journal of Geophysical Research: Solid Earth*, 118(8), 1–13. <https://doi.org/10.1002/jgrb.50288>
- Chouet, B., Dawson, P., Ohminato, T., Martini, M., Saccorotti, G., Giudicepietro, F., et al. (2003). Source mechanisms of explosions at Stromboli volcano, Italy, determined from moment-tensor inversions of very-long-period data. *Journal of Geophysical Research*, 108(B1), 2019. <https://doi.org/10.1029/2002JB001919>
- Civico, R., Ricci, T., Scarlato, P., Andronico, D., Cantarero, M., Carr, B. B., et al. (2021). Unoccupied Aircraft Systems (UASs) reveal the morphological changes at Stromboli Volcano (Italy) before, between, and after the 3 July and 28 August 2019 paroxysmal eruptions. *Remote Sensing*, 13(15), 2870. <https://doi.org/10.3390/rs13152870>
- Coppola, D., Cardone, D., Laiolo, M., Aveni, S., Campus, A., & Massimetti, F. (2023). Global radiant flux from active volcanoes: The 2000–2019 MIROVA database. *Frontiers in Earth Science*, 11, 1240107. <https://doi.org/10.3389/feart.2023.1240107>
- Coppola, D., Laiolo, M., Cigolini, C., Delle Donne, D., & Ripepe, M. (2016). Enhanced volcanic hot-spot detection using MODIS IR data: Results from the MIROVA system. In A. J. L. Harris, T. De Groeve, F. Garel, & S. A. Carn (Eds.), *Detecting, modelling and responding to effusive eruptions* (Vol. 426(1), pp. 181–205). Geological Society, London, Special Publications. <https://doi.org/10.1144/SP426.5>
- Coppola, D., Laiolo, M., Cigolini, C., Massimetti, F., Delle Donne, D., Ripepe, M., et al. (2020). Thermal remote sensing for global volcano monitoring experiences from the Mirova system. *Frontiers in Earth Science*, 7, 362. <https://doi.org/10.3389/feart.2019.00362>
- Coppola, D., Laiolo, M., Delle Donne, D., Ripepe, M., & Cigolini, C. (2014). Hot-spot detection and characterization of Strombolian activity from MODIS infrared data. *International Journal of Remote Sensing*, 35(9), 3403–3426. <https://doi.org/10.1080/01431161.2014.903354>
- Coppola, D., Laiolo, M., Massimetti, F., & Cigolini, C. (2019). Monitoring endogenous growth of open-vent volcanoes by balancing thermal and SO<sub>2</sub> emissions data derived from space. *Scientific Reports*, 9(1), 9394. <https://doi.org/10.1038/s41598-019-45753-4>
- Coppola, D., Piscopo, D., Laiolo, M., Cigolini, C., Delle Donne, D., & Ripepe, M. (2012). Radiative heat power at Stromboli volcano during 2000–2011: Twelve years of MODIS observations. *Journal of Volcanology and Geothermal Research*, 215–216, 48–60. <https://doi.org/10.1016/j.jvolgeores.2011.12.001>
- Coppola, D., Valade, S., Masias, P., Laiolo, M., Massimetti, F., Campus, A., et al. (2022). Shallow magma convection evidenced by excess degassing and thermal radiation during the dome-forming Sabancaya eruption (2012–2020). *Bulletin of Volcanology*, 84(2), 16. <https://doi.org/10.1007/s00445-022-01523-1>
- Delle Donne, D., Lo Coco, E., Bitetto, M., La Monica, F. P., Lacanna, G., Lages, J., et al. (2022). Spatio-temporal changes in degassing behavior at Stromboli volcano derived from two co-exposed SO<sub>2</sub> camera stations. *Frontiers in Earth Science*, 10, 972071. <https://doi.org/10.3389/feart.2022.972071>
- Delle Donne, D., & Ripepe, M. (2012). High-frame rate thermal imagery of Strombolian explosions: Implications for explosive and infrasonic source dynamics. *Journal of Geophysical Research*, 117(B9), B09206. <https://doi.org/10.1029/2011JB008987>
- Delle Donne, D., Tamburello, G., Aiuppa, A., Bitetto, M., Lacanna, G., D'Aleo, R., & Ripepe, M. (2017). Exploring the explosive-effusive transition using permanent ultraviolet cameras. *Journal of Geophysical Research: Solid Earth*, 122(6), 4377–4394. <https://doi.org/10.1002/2017JB014027>
- Di Lieto, B., Romano, P., Scarpa, R., & Linde, A. T. (2020). Strain signals before and during paroxysmal activity at Stromboli volcano, Italy. *Geophysical Research Letters*, 47(21), e2020GL088521. <https://doi.org/10.1029/2020GL088521>
- Di Stefano, F., Mollo, S., Ubide, T., Petrone, C. M., Caulfield, J., Scarlato, P., et al. (2020). Mush cannibalism and disruption recorded by clinopyroxene phenocrysts at Stromboli volcano: New insights from recent 2003–2017 activity. *Lithos*, 360–361, 105440. <https://doi.org/10.1016/j.lithos.2020.105440>
- Di Traglia, F., Calvari, S., D'Auria, L., Nolesini, T., Bonaccorso, A., Fornaciai, A., et al. (2018). The 2014 effusive eruption at Stromboli: New insights from in situ and remote-sensing measurements. *Remote Sensing*, 10(12), 2035. <https://doi.org/10.3390/rs10122035>
- Di Traglia, F., Nolesini, T., Ciampalini, A., Solari, L., Frodella, W., Bellotti, F., et al. (2018). Tracking morphological changes and slope instability using spaceborne and ground-based SAR data. *Geomorphology*, 300, 95–112. <https://doi.org/10.1016/j.geomorph.2017.10.023>
- Edmonds, M., Liu, E., & Cashman, K. (2022). Open-vent volcanoes fuelled by depth-integrated magma degassing. *Bulletin of Volcanology*, 84(3), 28. <https://doi.org/10.1007/s00445-021-01522-8>
- Fisher, D., & Wooster, M. J. (2018). Shortwave IR adaption of the mid-infrared radiance method of Fire Radiative Power (FRP) retrieval for assessing industrial gas flaring output. *Remote Sensing*, 10(2), 305. <https://doi.org/10.3390/rs10020305>
- Flynn, L. P., Harris, A. J. L., & Wright, R. (2001). Improved identification of volcanic features using Landsat 7 ETM+. *Remote Sensing of Environment*, 78(1), 180–193. [https://doi.org/10.1016/S0034-4257\(01\)00258-9](https://doi.org/10.1016/S0034-4257(01)00258-9)
- Francalanci, L., Tommasini, S., Conticelli, S., & Davies, G. R. (1999). Sr isotope evidence for short magma residence time for the 20th century at Stromboli volcano, Italy. *Earth and Planetary Science Letters*, 167(1–2), 61–69. [https://doi.org/10.1016/S0012-821X\(99\)00013-8](https://doi.org/10.1016/S0012-821X(99)00013-8)
- Francis, P., Oppenheimer, C., & Stevenson, D. (1993). Endogenous growth of persistently active volcanoes. *Nature*, 366(6455), 554–557. <https://doi.org/10.1038/366554a0>
- Francis, P. W. (1979). Infra-red techniques for volcano monitoring and prediction - A review. *Journal of the Geological Society*, 136(3), 355–359. <https://doi.org/10.1144/gsjgs.136.3.0355>
- Ganci, G., Bilotta, G., Cappello, A., Hérault, A., & Del Negro, C. (2016). HOTSAT: A multiplatform system for the satellite thermal monitoring of volcanic activity. In A. J. L. Harris, T. De Groeve, F. Garel, & S. A. Carn (Eds.), *Detecting, modelling and responding to effusive eruptions* (Vol. 426(1), pp. 207–221). Geological Society, London, Special Publications. <https://doi.org/10.1144/SP426.21>

- Ganci, G., Vicari, A., Fortuna, L., & Del Negro, C. (2011). The HOTSAT volcano monitoring system based on a combined use of SEVIRI and MODIS multispectral data. *Annals of Geophysics*, *54*, 544–550. <https://doi.org/10.4401/ag-5338>
- Gaonac'h, H., Vandemeulebrouck, J., Stix, J., & Halbwachs, M. (1994). Thermal infrared satellite measurements of volcanic activity at Stromboli and Vulcano. *Journal of Geophysical Research*, *99*(B5), 9477–9485. <https://doi.org/10.1029/93JB02392>
- Gaudin, D., Taddeucci, J., Scarlato, P., Del Bello, E., Ricci, T., Orr, T., et al. (2017). Integrating puffing and explosions in a general scheme for Strombolian-style activity. *Journal of Geophysical Research: Solid Earth*, *122*(3), 1860–1875. <https://doi.org/10.1002/2016JB013707>
- Genzano, N., Marchese, F., Plank, S., & Pergola, N. (2023). Monitoring the Mauna Loa (Hawaii) eruption of November–December 2022 from space: Results from GOES-R, Sentinel-2 and Landsat-8/9 observations. *International Journal of Applied Earth Observation and Geo-information*, *122*, 103388. <https://doi.org/10.1016/j.jag.2023.103388>
- Genzano, N., Pergola, N., & Marchese, F. (2020). A Google Earth Engine Tool to investigate, map and monitor volcanic thermal anomalies at global scale by means of mid-high spatial resolution satellite data. *Remote Sensing*, *12*(19), 3232. <https://doi.org/10.3390/rs12193232>
- Giberti, G., Jaupart, C., & Sartoris, G. (1992). Steady-state operation of Stromboli volcano, Italy: Constraints on the feeding system. *Bulletin of Volcanology*, *54*(7), 535–541. <https://doi.org/10.1007/BF00569938>
- Giordano, G., & De Astis, G. (2021). The summer 2019 basaltic Vulcanian eruptions (paroxysms) of Stromboli. *Bulletin of Volcanology*, *83*, 1. <https://doi.org/10.1007/s00445-020-01423-2>
- Giudicepietro, F., Calvari, S., Alparone, S., Bianco, F., Bonaccorso, A., Bruno, V., et al. (2019). Integration of ground-based remote-sensing and in situ multidisciplinary monitoring data to analyze the eruptive activity of Stromboli Volcano in 2017–2018. *Remote Sensing*, *11*(15), 1813. <https://doi.org/10.3390/rs11151813>
- Giudicepietro, F., Calvari, S., De Cesare, W., Di Lieto, B., Di Traglia, F., Esposito, A. M., et al. (2023). Seismic and thermal precursors of crater collapses and overflows at Stromboli volcano. *Scientific Reports*, *13*(1), 11115. <https://doi.org/10.1038/s41598-023-38205-7>
- Giudicepietro, F., López, C., Macedonio, G., Alparone, S., Bianco, F., Calvari, S., et al. (2020). Geophysical precursors of the July–August 2019 paroxysmal eruptive phase and their implications for Stromboli volcano (Italy) monitoring. *Scientific Reports*, *10*(1), 10296. <https://doi.org/10.1038/s41598-020-67220-1>
- Harris, A. J. L. (2013). *Thermal remote sensing of active volcanoes: A user's manual*. Cambridge University Press. <https://doi.org/10.1017/CBO9781139029346>
- Harris, A. J. L., Donne, D. D., Dehn, J., Ripepe, M., & Worden, A. K. (2013). Volcanic plume and bomb field masses from thermal infrared camera imagery. *Earth and Planetary Science Letters*, *365*, 77–85. <https://doi.org/10.1016/j.epsl.2013.01.004>
- Harris, A. J. L., & Ripepe, M. (2007). Synergy of multiple geophysical approaches to unravel explosive eruption conduit and source dynamics – A case study from Stromboli. *Geochemistry*, *67*, 1–35. <https://doi.org/10.1016/j.chemer.2007.01.003>
- Harris, A. J. L., Stevens, N. F., Maciejewski, A. J. H., & Röhlín, P. J. (1996). Thermal evidence for linked vents at Stromboli. *Acta Vulcanologica*, *8*, 57–62.
- Harris, A. J. L., & Stevenson, D. S. (1997a). Magma budgets and steady-state activity of Vulcano and Stromboli volcanoes. *Geophysical Research Letters*, *24*(9), 1043–1046. <https://doi.org/10.1029/97GL00861>
- Harris, A. J. L., & Stevenson, D. S. (1997b). Thermal observations of degassing open conduits and fumaroles at Stromboli and Vulcano using remotely sensed data. *Journal of Volcanology and Geothermal Research*, *76*(3–4), 175–198. [https://doi.org/10.1016/S0377-0273\(96\)00097-2](https://doi.org/10.1016/S0377-0273(96)00097-2)
- Houghton, B. F., & Gonnermann, H. M. (2008). Basaltic explosive volcanism: Constraints from deposits and models. *Geochemistry*, *68*(2), 117–140. <https://doi.org/10.1016/j.chemer.2008.04.002>
- Hu, X., Ban, Y., & Nascetti, A. (2021). Sentinel-2 MSI data for active fire detection in major fire-prone biomes: A multi-criteria approach. *International Journal of Applied Earth Observation and Geoinformation*, *101*, 102347. <https://doi.org/10.1016/j.jag.2021.102347>
- Johnson, J. B., Watson, L. M., Palma, J. L., Dunham, E. M., & Anderson, J. F. (2018). Forecasting the eruption of an open-vent volcano using resonant infrasonic tones. *Geophysical Research Letters*, *45*(5), 2213–2220. <https://doi.org/10.1002/2017GL076506>
- Kazahaya, K., Shinohara, H., & Saito, G. (1994). Excessive degassing of Izu-Oshima volcano: Magma convection in a conduit. *Bulletin of Volcanology*, *56*(3), 207–216. <https://doi.org/10.1007/BF00279605>
- Laiolo, M., Campus, A., Massimetti, F., & Coppola, D. (2023). Twenty years of space-based MIR-data at Stromboli volcano: Relation between thermal regimes and eruptive activity, XXVIII General Assembly of the International Union of Geodesy and Geophysics (IUGG) (Berlin 2023). <https://doi.org/10.57757/IUGG23-1104>
- Laiolo, M., Delle Donne, D., Coppola, D., Bitetto, M., Cigolini, C., Schiava, D., et al. (2022). Shallow magma dynamics at open-vent volcanoes tracked by coupled thermal and SO<sub>2</sub> observations. *Earth and Planetary Science Letters*, *594*, 117726. <https://doi.org/10.1016/j.epsl.2022.117726>
- Laiolo, M., Ripepe, M., Cigolini, C., Coppola, D., Della Schiava, M., Genco, R., et al. (2019). Space- and ground-based geophysical data tracking of magma migration in shallow feeding system of Mount Etna Volcano. *Remote Sensing*, *11*(10), 1182. <https://doi.org/10.3390/rs11101182>
- Landi, P., Marchetti, E., La Felice, S., Ripepe, M., & Rosi, M. (2011). Integrated petrochemical and geophysical data reveals thermal distribution of the feeding conduits at Stromboli volcano, Italy. *Geophysical Research Letters*, *38*(8), L08305. <https://doi.org/10.1029/2010GL046296>
- Layana, S., Aguilera, F., Rojo, G., Vergara, Á., Salazar, P., Quispe, J., et al. (2020). Volcanic anomalies monitoring system (VOLCANOMS), a low-cost volcanic monitoring system based on Landsat images. *Remote Sensing*, *12*(10), 1589. <https://doi.org/10.3390/rs12101589>
- Marchese, F., Coppola, D., Falconieri, A., Genzano, N., & Pergola, N. (2022). Investigating phases of thermal unrest at Ambrym (Vanuatu) Volcano through the normalized hot spot indices tool and the integration with the MIROVA system. *Remote Sensing*, *14*(13), 3136. <https://doi.org/10.3390/rs14133136>
- Marchese, F., Genzano, N., Neri, M., Falconieri, A., Mazzeo, G., & Pergola, N. (2019). A multi-channel algorithm for mapping volcanic thermal anomalies by means of Sentinel-2 MSI and Landsat-8 OLI data. *Remote Sensing*, *11*(23), 2876. <https://doi.org/10.3390/rs11232876>
- Marchese, F., Genzano, N., Nolde, M., Falconieri, A., Pergola, N., & Plank, S. (2022). Mapping and characterizing the Kilauea (Hawai'i) lava lake through Sentinel-2 MSI and Landsat-8 OLI observations of December 2020–February 2021. *Environmental Modelling & Software*, *148*, 105273. <https://doi.org/10.1016/j.envsoft.2021.105273>
- Marchese, F., Neri, M., Falconieri, A., Lacava, T., Mazzeo, G., Pergola, N., & Tramutoli, V. (2018). The contribution of multi-sensor infrared satellite observations to monitor Mt. Etna (Italy) activity during May to August 2016. *Remote Sensing*, *10*(12), 1948. <https://doi.org/10.3390/rs10121948>
- Marchetti, E., & Ripepe, M. (2005). Stability of the seismic source during effusive and explosive activity at Stromboli Volcano. *Geophysical Research Letters*, *32*(3), L03307. <https://doi.org/10.1029/2004GL021406>
- Marotta, E., Calvari, S., Cristaldi, A., D'Auria, L., Di Vito, M. A., Moretti, R., et al. (2015). Reactivation of Stromboli's summit craters at the end of the 2007 effusive eruption detected by thermal surveys and seismicity. *Journal of Geophysical Research: Solid Earth*, *120*(11), 7376–7395. <https://doi.org/10.1002/2015JB012288>



- Marsella, M., Baldi, P., Coltelli, M., & Fabris, M. (2012). The morphological evolution of the Sciarra del Fuoco since 1868: Reconstructing the effusive activity at Stromboli volcano. *Bulletin of Volcanology*, 74(1), 231–248. <https://doi.org/10.1007/s00445-011-0516-6>
- Massimetti, et al. (2024). Stromboli craters heat flux (VRPSWIR) dataset from SWIR Sentinel-2, Landsat-8 & -9 [Dataset] OSF. <https://osf.io/zdbyq/>
- Massimetti, F., Coppola, D., Laiolo, M., Valade, S., Cigolini, C., & Ripepe, M. (2020). Volcanic hot-spot detection using SENTINEL-2: A comparison with MODIS-MIROVA thermal data series. *Remote Sensing*, 12(5), 820. <https://doi.org/10.3390/rs12050820>
- Mattia, M., Di Lieto, B., Ganci, G., Bruno, V., Romano, P., Ciancitto, F., et al. (2021). The 2019 eruptive activity at Stromboli Volcano: A multidisciplinary approach to reveal hidden features of the “unexpected” 3 July paroxysm. *Remote Sensing*, 13(20), 4064. <https://doi.org/10.3390/rs13204064>
- McGreger, A. D., & Lees, J. M. (2004). Vent discrimination at Stromboli volcano, Italy. *Journal of Volcanology and Geothermal Research*, 137(1–3), 169–185. <https://doi.org/10.1016/j.jvolgeores.2004.05.007>
- Mercalli, G. (1907). *I vulcani attivi della Terra*. Hoepli.
- Métrich, N., Bertagnini, A., & Di Muro, A. (2010). Conditions of magma storage, degassing and ascent at Stromboli: New insights into the volcano plumbing system with inference on the eruptive dynamics. *Journal of Petrology*, 51(3), 603–626. <https://doi.org/10.1093/petrology/egp083>
- Métrich, N., Bertagnini, A., Landi, P., & Rosi, M. (2001). Crystallization driven by decompression and water loss at Stromboli volcano (Aeolian Islands, Italy). *Journal of Petrology*, 42(8), 1471–1490. <https://doi.org/10.1093/petrology/42.8.1471>
- Métrich, N., Bertagnini, A., & Pistolesi, M. (2021). Paroxysms at Stromboli volcano (Italy): Source, genesis and dynamics. *Frontiers in Earth Science*, 9, 593339. <https://doi.org/10.3389/feart.2021.593339>
- Mia, M. B., Fujimitsu, Y., & Nishijima, J. (2018). Monitoring of thermal activity at the Hatchobaru–Otake geothermal area in Japan using multi-source satellite images—With comparisons of methods, and solar and seasonal effects. *Remote Sensing*, 10(9), 1430. <https://doi.org/10.3390/rs10091430>
- Morfitt, R., Barsi, J., Levy, R., Markham, B., Micijevic, E., Ong, L., et al. (2015). Landsat-8 Operational Land Imager (OLI) radiometric performance on-orbit. *Remote Sensing*, 7(2), 2208–2237. <https://doi.org/10.3390/rs70202208>
- Németh, K., & Cronin, S. J. (2008). Volcanic craters, pit craters and high-level magma-feeding systems of a mafic island-arc volcano: Ambrym, Vanuatu, South Pacific. In K. Thomson & N. Petford (Eds.), *Structure and emplacement of high-level magmatic systems* (Vol. 302(1), pp. 87–102). Geological Society, London, Special Publications. <https://doi.org/10.1144/sp302.6>
- Oppenheimer, C., Rothery, D. A., & Francis, P. W. (1993). Thermal distributions at fumarole fields - Implications for infrared remote-sensing of active volcanoes. *Journal of Volcanology and Geothermal Research*, 55(1–2), 97–115. [https://doi.org/10.1016/0377-0273\(93\)90092-6](https://doi.org/10.1016/0377-0273(93)90092-6)
- Patrick, M. R., Harris, A. J. L., Ripepe, M., Dehn, J., Rothery, D. A., & Calvari, S. (2007). Strombolian explosive styles and source conditions: Insights from thermal (FLIR) video. *Bulletin of Volcanology*, 69(7), 769–784. <https://doi.org/10.1007/s00445-006-0107-0>
- Petrone, C. M., Mollo, S., Gertisser, R., Buret, Y., Scarlato, P., Del Bello, E., et al. (2022). Magma recharge and mush rejuvenation drive paroxysmal activity at Stromboli volcano. *Nature Communication*, 13(1), 7717. <https://doi.org/10.1038/s41467-022-35405-z>
- Phillipson, G., Sobradelo, R., & Gottsmann, J. (2013). Global volcanic unrest in the 21st century: An analysis of the first decade. *Journal of Volcanology and Geothermal Research*, 264, 183–196. <https://doi.org/10.1016/j.jvolgeores.2013.08.004>
- Pioli, L., Pistolesi, M., & Rosi, M. (2014). Transient explosions at open-vent volcanoes: The case of Stromboli (Italy). *Geology*, 133(10), 429–866. <https://doi.org/10.1130/G35844.1>
- Pistolesi, M., Delle Donne, D., Pioli, L., Rosi, M., & Ripepe, M. (2011). The 15 March 2007 explosive crisis at Stromboli volcano, Italy: Assessing physical parameters through a multidisciplinary approach. *Journal of Geophysical Research: Solid Earth*, 116(B12), B12206. <https://doi.org/10.1029/2011JB008527>
- Plank, S., Marchese, F., Filizzola, C., Pergola, N., Neri, M., Nolde, M., & Martinis, S. (2019). The July/August 2019 Lava Flows at the Sciarra del Fuoco, Stromboli—Analysis from Multi-Sensor Infrared Satellite Imagery. *Remote Sensing*, 11(23), 2879. <https://doi.org/10.3390/rs11232879>
- Ramsey, M. S., & Harris, A. J. L. (2013). Volcanology 2020: How will thermal remote sensing of volcanic surface activity evolve over the next decade? (invited review article). *Journal of Volcanology and Geothermal Research*, 249, 217–233. <https://doi.org/10.1016/j.jvolgeores.2012.05.011>
- Ramsey, M. S., Harris, A. J. L., & Watson, I. M. (2022). Volcanology 2030: Will an orbital volcano observatory finally become a reality? *Bulletin of Volcanology*, 84(1), 6. <https://doi.org/10.1007/s00445-021-01501-z>
- Reath, K., Pritchard, M., Poland, M., Delgado, F., Carn, S., Coppola, D., et al. (2019). Thermal, deformation, and degassing remote sensing time series (CE 2000–2017) at the 47 most active volcanoes in Latin America: Implications for volcanic systems. *Journal of Geophysical Research: Solid Earth*, 124(1), 195–218. <https://doi.org/10.1029/2018JB016199>
- Reiss, M. C., Massimetti, F., Laizer, A. S., Campus, A., Rumpker, G., & Kazimoto, E. O. (2023). Overview of seismo-acoustic tremor at Oldoinyo Lengai, Tanzania: Shallow storage and eruptions of carbonatite melt. *Journal of Volcanology and Geothermal Research*, 442, 107898. <https://doi.org/10.1016/j.jvolgeores.2023.107898>
- Ripepe, M., Delle Donne, D., Harris, A. J. L., Marchetti, E., & Ulivieri, G. (2008). Dynamics of strombolian activity. In S. Calvari, S. Inguaggiato, G. Puglisi, M. Ripepe, & M. Rosi (Eds.), *The Stromboli Volcano: An integrated study of the 2002–2003 eruption, geophysics monograph series* (Vol. 182, pp. 39–48). American Geophysical Union. <https://doi.org/10.1029/182GM05>
- Ripepe, M., Delle Donne, D., Lacanna, G., Marchetti, E., & Ulivieri, G. (2009). The onset of the 2007 Stromboli effusive eruption recorded by an integrated geophysical network. *Journal of Volcanology and Geothermal Research*, 182(3–4), 131–136. <https://doi.org/10.1016/j.jvolgeores.2009.02.011>
- Ripepe, M., Delle Donne, D., Legrand, D., Valade, S., & Lacanna, G. (2021). Magma pressure discharge induces very long period seismicity. *Scientific Reports*, 11(1), 20065. <https://doi.org/10.1038/s41598-021-99513-4>
- Ripepe, M., Harris, A. J. L., & Marchetti, E. (2005). Coupled thermal oscillations in explosive activity at different craters of Stromboli volcano. *Geophysical Research Letters*, 32(17), L17302. <https://doi.org/10.1029/2005GL022711>
- Ripepe, M., Lacanna, G., Pistolesi, M., Silengo, M. C., Aiuppa, A., Laiolo, M., et al. (2021). Ground deformation reveals the scale-invariant conduit dynamics driving explosive basaltic eruptions. *Nature Communication*, 12(1), 1683. <https://doi.org/10.1038/s41467-021-21722-2>
- Ripepe, M., & Marchetti, E. (2002). Array tracking of infrasonic sources at Stromboli volcano. *Geophysical Research Letters*, 29(22), 2076. <https://doi.org/10.1029/2002GL015452>
- Ripepe, M., Marchetti, E., Delle Donne, D., Genco, R., Innocenti, L., Lacanna, G., & Valade, S. (2018). Infrasonic early warning system for explosive eruptions. *Journal of Geophysical Research: Solid Earth*, 123(11), 9570–9585. <https://doi.org/10.1029/2018JB015561>
- Ripepe, M., Marchetti, E., & Ulivieri, G. (2007). Infrasonic monitoring at Stromboli volcano during the 2003 effusive eruption: Insights on the explosive and degassing process of an open conduit system. *Journal of Geophysical Research*, 112(B9), B09207. <https://doi.org/10.1029/2006JB004613>



- Ripepe, M., Pistolesi, M., Coppola, D., Delle Donne, D., Genco, R., Lacanna, G., et al. (2017). Forecasting effusive dynamics and decompression rates by magmatic model at open-vent volcanoes. *Scientific Reports*, 7(1), 3885. <https://doi.org/10.1038/s41598-017-03833-3>
- Rittmann, A. (1931). Der ausbruch des Stromboli am 11 September 1930. *Zeitschrift für vulkanologie*, 14, 47–77.
- Rose, W. I., Palma, J. L., Delgado Granados, H., & Varley, N. (2013). Open-vent volcanism and related hazards: Overview. In W. I. Rose, J. L. Palma, H. Delgado Granados, & N. Varley (Eds.), *Understanding open-vent volcanism and related hazards* (Vol. 498, pp. 7–13). Special Papers Geological Society of America. [https://doi.org/10.1130/2013.2498\(00](https://doi.org/10.1130/2013.2498(00)
- Rosi, M., Bertagnini, A., Harris, A. J. L., Pioli, L., Pistolesi, M., & Ripepe, M. (2006). A case history of paroxysmal explosion at Stromboli: Timing and dynamics of the April 5, 2003 event. *Earth and Planetary Science Letters*, 243(3–4), 594–606. <https://doi.org/10.1016/j.epsl.2006.01.035>
- Rosi, M., Bertagnini, A., & Landi, P. (2000). Onset of the persistent activity at Stromboli Volcano (Italy). *Bulletin of Volcanology*, 62(4–5), 294–300. <https://doi.org/10.1007/s004450000098>
- Rosi, M., Pistolesi, M., Bertagnini, A., Landi, P., Pompilio, M., & Di Roberto, A. (2013). Stromboli volcano, Aeolian Islands (Italy): Present eruptive activity and hazards. In F. Lucchi, A. Peccerillo, J. Keller, C. A. Tranne, & P. L. Rossi (Eds.), *The Aeolian islands volcanoes* (Vol. 37(1), pp. 473–490). Geological Society, London, Memoirs. <https://doi.org/10.1144/M37.14>
- Rothery, D. A., Francis, P. W., & Wood, C. A. (1988). Volcano monitoring using short wavelength infrared data from satellites. *Journal of Geophysical Research*, 93(B7), 7993–8008. <https://doi.org/10.1029/JB093iB07p07993>
- Salvatore, V., Silleni, A., Corneli, D., Taddeucci, J., Palladino, D. M., Sottili, G., et al. (2018). Parameterizing multi-vent activity at Stromboli Volcano (Aeolian Islands, Italy). *Bulletin of Volcanology*, 80(7), 64. <https://doi.org/10.1007/s00445-018-1239-8>
- Scharff, L., Hort, M., Harris, A. J. L., Ripepe, M., Lees, J. M., & Seyfried, R. (2008). Eruption dynamics of the SW crater of Stromboli volcano, Italy: An interdisciplinary approach. *Journal of Volcanology and Geothermal Research*, 176(4), 565–570. <https://doi.org/10.1016/j.jvolgeores.2008.05.008>
- Shephard, M. W., & Kennelly, E. J. (2003). Effect of band-to-band coregistration on fire property retrievals. *IEEE Transactions on Geoscience and Remote Sensing*, 41(11), 2648–2661. <https://doi.org/10.1109/TGRS.2003.814912>
- Shevchenko, A. V., Dvigalo, V. N., Zorn, E. U., Vassileva, M. S., Massimetti, F., Walter, T. R., et al. (2021). Constructive and destructive processes during the 2018–2019 eruption episode at Shiveluch Volcano, Kamchatka, studied from satellite and Aerial data. *Frontiers in Earth Science*, 9, 680051. <https://doi.org/10.3389/feart.2021.680051>
- Shinohara, H. (2008). Excess degassing from volcanoes and its role on eruptive and intrusive activity. *Reviews of Geophysics*, 46(4), RG4005. <https://doi.org/10.1029/2007RG000244>
- Simons, B. C., Jolly, A. D., Eccles, J. D., & Cronin, S. J. (2020). Spatiotemporal relationships between two closely-spaced Strombolian-style vents, Yasur, Vanuatu. *Geophysical Research Letters*, 47(5), e2019GL085687. <https://doi.org/10.1029/2019GL085687>
- Smittarello, D., Smets, B., Barrière, J., Michellier, C., Oth, A., Shreve, T., et al. (2022). Precursor-free eruption triggered by edifice rupture at Nyiragongo volcano. *Nature*, 609(7925), 83–88. <https://doi.org/10.1038/s41586-022-05047-8>
- Spampinato, L., Calvari, S., Oppenheimer, C., & Lodato, L. (2008). Shallow magma transport for the 2002–03 Mt. Etna eruption inferred from thermal infrared surveys. *Journal of Volcanology and Geothermal Research*, 177(2), 301–312. <https://doi.org/10.1016/j.jvolgeores.2008.05.013>
- Sparks, R. (2003). Forecasting volcanic eruptions. *Earth and Planetary Science Letters*, 210(1–2), 1–15. [https://doi.org/10.1016/S0012-821X\(03\)00124-9](https://doi.org/10.1016/S0012-821X(03)00124-9)
- Sugimura, S., Nishimura, T., Lacanna, G., Legrand, D., Valade, S., & Ripepe, M. (2021). Seismic source migration during Strombolian eruptions inferred by very-near-field broadband seismic network. *Journal of Geophysical Research: Solid Earth*, 126(12), e2021JB022623. <https://doi.org/10.1029/2021JB022623>
- Tamburello, G., Aiuppa, A., Kantzas, E. P., McGonigle, A. J. S., & Ripepe, M. (2012). Passive vs. active degassing modes at an open-vent volcano (Stromboli, Italy). *Earth and Planetary Science Letters*, 359–360, 106–116. <https://doi.org/10.1016/j.epsl.2012.09.050>
- Tibaldi, A., Corazzato, C., Apuani, T., Pasquaré, F. A., & Vezzoli, L. (2008). Geological-structural framework of Stromboli volcano, past collapses, and possible influence on the events of the 2002–2003 crisis. In S. Calvari, S. Inguaggiato, G. Puglisi, M. Ripepe, & M. Rosi (Eds.), *The Stromboli Volcano: An integrated study of the 2002–2003 eruption*, *Geophysics Monograph Series* (Vol. 182, pp. 5–17). American Geophysical Union. <https://doi.org/10.1029/182GM03>
- Tilling, R. I. (2008). The critical role of volcano monitoring in risk reduction. *Advances in Geosciences*, 14, 3–11. <https://doi.org/10.5194/adgeo-14-3-2008>
- Valade, S., Coppola, D., Campion, R., Ley, A., Boulesteix, T., Taquet, N., et al. (2023). Lava dome cycles reveal rise and fall of magma column at Popocatepetl volcano. *Nature Communications*, 14(1), 3254. <https://doi.org/10.1038/s41467-023-38386-9>
- Valade, S., Lacanna, G., Coppola, D., Laiolo, M., Pistolesi, M., Delle Donne, D., et al. (2016). Tracking dynamics of magma migration in open-conduit systems. *Bulletin of Volcanology*, 78(11), 78. <https://doi.org/10.1007/s00445-016-1072-x>
- Valade, S., Ley, A., Massimetti, F., D'Hondt, O., Laiolo, M., Coppola, D., et al. (2019). Towards global volcano monitoring using multisensor sentinel missions and Artificial Intelligence: The MOUNTS monitoring system. *Remote Sensing*, 11(13), 1528. <https://doi.org/10.3390/rs11131528>
- van Manen, S. M., Dehn, J., & Blake, S. (2010). Satellite thermal observations of the Bezymianny lava dome 1993–2008: Precursory activity, large explosions, and dome growth. *Journal of Geophysical Research*, 115(B8), B08205. <https://doi.org/10.1029/2009JB006966>
- Vergnolle, S., & Métrich, N. (2021). Open-vent volcanoes: A preface to the special issue. *Bulletin of Volcanology*, 83(5), 29. <https://doi.org/10.1007/s00445-021-01454-3>
- Vergnolle, S., & Métrich, N. (2022). An interpretative view of open-vent volcanoes. *Bulletin of Volcanology*, 84(9), 83. <https://doi.org/10.1007/s00445-022-01581-5>
- Viccaro, M., Cannata, A., Cannavò, F., De Rosa, R., Giuffrida, M., Nicotra, E., et al. (2021). Shallow conduit dynamics fuel the unexpected paroxysms of Stromboli volcano during the summer 2019. *Scientific Reports*, 11(1), 266. <https://doi.org/10.1038/s41598-020-79558-7>
- Voloschina, M., Métrich, N., Bertagnini, A., Marianelli, P., Aiuppa, A., Ripepe, M., & Pistolesi, M. (2023). Explosive eruptions at Stromboli volcano (Italy): A comprehensive geochemical view on magma sources and intensity range. *Bulletin of Volcanology*, 85(6), 1–21. <https://doi.org/10.1007/s00445-023-01647-y>
- Washington, H. S. (1917). Persistence of vents at Stromboli and its bearing on volcanic mechanism. *Geological Society of America Bulletin*, 28(1), 248–278. <https://doi.org/10.1130/gsab-28-249>
- Woitischek, J., Woods, A. W., Edmonds, M., Oppenheimer, C., Aiuppa, A., Pering, T. D., et al. (2020). Strombolian eruptions and dynamics of magma degassing at Yasur Volcano (Vanuatu). *Journal of Volcanology and Geothermal Research*, 398, 106869. <https://doi.org/10.1016/j.jvolgeores.2020.106869>

- Wooster, M. J., Zhukov, B., & Oertel, D. (2003). Fire radiative energy for quantitative study of biomass burning: Derivation from the BIRD experimental satellite and comparison to MODIS fire products. *Remote Sensing of Environments*, 86(1), 83–107. [https://doi.org/10.1016/S0034-4257\(03\)00070-1](https://doi.org/10.1016/S0034-4257(03)00070-1)
- Worden, A., Dehn, J., & Webley, P. (2014). Frequency based satellite monitoring of small scale explosive activity at remote north Pacific volcanoes. *Journal of Volcanology and Geothermal Research*, 286, 1–14. <https://doi.org/10.1016/j.jvolgeores.2014.08.019>
- Wright, R., Blackett, M., & Hill-Butler, C. (2015). Some observations regarding the thermal flux from Earth's erupting volcanoes for the period of 2000 to 2014. *Geophysical Research Letters*, 42(2), 282–289. <https://doi.org/10.1002/2014GL061997>
- Wright, R., Flynn, L., Garbeil, H., Harris, A. J. L., & Pilger, E. (2002). Automated volcanic eruption detection using MODIS. *Remote Sensing of Environments*, 82(1), 135–155. [https://doi.org/10.1016/S0034-4257\(02\)00030-5](https://doi.org/10.1016/S0034-4257(02)00030-5)
- Wright, R., & Flynn, L. P. (2003). On the retrieval of lava-flow surface temperatures from infrared satellite data. *Geology*, 31(10), 893–896. <https://doi.org/10.1130/G19645.1>
- Wright, R., & Pilger, E. (2008). Radiant flux from Earth's subaerially erupting volcanoes. *International Journal of Remote Sensing*, 29(22), 6443–6466. <https://doi.org/10.1080/01431160802168210>
- Yokoyama, I. (1972). Heat and mass transfer through volcanoes. *Rivista Italiana di Geofisica*, 21, 165–169.
- Zakšek, K., Hort, M., & Lorenz, E. (2015). Satellite and ground based thermal observation of the 2014 effusive eruption at Stromboli Volcano. *Remote Sensing*, 7(12), 17190–17211. <https://doi.org/10.3390/rs71215876>
- Zanon, V., Neri, M., & Pecora, E. (2009). Interpretation of data from the monitoring thermal camera of Stromboli volcano (Aeolian Islands, Italy). *Geological Magazine*, 46(4), 591–601. <https://doi.org/10.1017/S0016756809005937>
- Zuccarello, L., De Angelis, S., Minio, V., Saccorotti, G., Bean, C. J., Paratore, M., & Ibanez, J. M. (2022). Volcanic tremor tracks changes in multi-vent activity at Mt. Etna, Italy: Evidence from analyses of seismic array data. *Geophysical Research Letters*, 49(22), e2022GL100056. <https://doi.org/10.1029/2022GL100056>